Department of Physics and Astronomy
University of Heidelberg

Bachelor Thesis in Physics
submitted by

David Elsing

born in Freiburg im Breisgau (Germany)

2018

Plasma screening effects in laser-generated plasmas

This Bachelor Thesis has been carried out by David Elsing at the
Max Planck Institute for Nuclear Physics in Heidelberg
under the supervision of
PD Dr. Adriana Pálffy-Buß and Dr. Yuanbin Wu

Abstract

Plasma screening effects affect the rate at which nuclear reactions occur in hot and dense astrophysical plasmas. Their direct measurement in the laboratory has not succeeded so far and is vital for our understanding of nuclear processes occurring in stellar nucleosynthesis. A promising route for such measurements involve petawatt laser facilities capable of producing hot and dense plasmas in the laboratory. In this work, we consider and compare theoretically four plasma screening models originally introduced for astrophysical plasmas, and apply them to nuclear reactions in laser-generated plasmas for a large range of densities and temperatures. We consider two astrophysically relevant nuclear reactions, namely $^{13}\mathrm{C}(\alpha,\mathrm{n})\,^{16}\mathrm{O}$, which is one of the important helium burning processes in advanced stellar phases as well as one of the interesting neutron sources for the slow neutron caption process of nucleosynthesis, and $^{7}\mathrm{Li}(\mathrm{d},\alpha)\alpha$, which might be the key to explain the lithium production problem of the standard big bang nucleosynthesis. Our results anticipate experiments on nuclear reactions in plasmas being rendered possible at high power laser facilities such as the Extreme Light Infrastructure under construction today, and shedding light on the validity of plasma screening models.

Die Effekte der *Plasmaabschirmung* (*plasma screening*) beeinflussen die Rate von Kernreaktionen in heißen und dichten astrophysikalischen Plasmen. Eine direkte Messung im Labor war bisher nicht erfolgreich und ist wesentlich für unser Verständnis von nuklearen Prozessen, welche in der stellaren Nukleosynthese vorkommen. Eine vielversprechende Möglichkeit für solche Messungen beinhaltet Petawatt-Lasereinrichtungen, welche zur Produktion von heißen und dichten Plasmas im Labor fähig sind. In dieser Arbeit werden vier Modelle für Plasmaabschirmung, welche ursprünglich für astrophysikalische Plasmen eingeführt wurden, theoretisch betrachtet und verglichen, und auf Kernreaktionen in Laser-generierten Plasmen für eine weite Auswahl von Dichten und Temperaturen angewandt. Wir untersuchen die zwei astrophysikalisch relevanten Kernreaktionen $^{13}\mathrm{C}(\alpha,\mathrm{n})\,^{16}\mathrm{O}$, welches einer der wichtigen Heliumverbrennungsprozesse in fortgeschrittenen Sternphasen sowie eine der interessanten Neutronenquellen für den *s-Prozess* der Nukleosynthese ist, sowie $^{7}\mathrm{Li}(\mathrm{d},\alpha)\alpha$, was der Schlüssel zur Erklärung des Problems der Lithiumproduktion in der Standard-Urknall-Nukleosynthese sein könnte. Unsere Ergebnisse wurden in der Erwartung berechnet, dass Experimente an Kernreaktionen in Plasmen an Hochenergie-Lasereinrichtungen möglich sein werden, wie z.B. die Extreme Light Infrastructure, welche sich heute im Bau befindet. Dies könnte über die Gültigkeit der Plasmaabschirmungsmodelle aufklären.

1 Introduction

A *plasma* is an ionized gas — a fundamental state of matter besides solids, liquids and non-ionized gases. For the definition used here, the ionization is strong enough for the plasma to be highly electrically conductive. Through the charge separation, macroscopic currents and magnetic fields can occur and influence the macroscopic dynamics of the plasma [1].

Plasmas can be generated by heating a gas to the extent that the thermal energy is large enough for ionization to occur. The most prominent example for this are stars, where the thermal energy is commonly larger than the ionization energy of the plasma constituents, making plasma the most abundant form of matter in the observable universe. Stars consist of plasma because of their high temperature, which is mainly sustained through thermonuclear reactions. In turn, the rates of these nuclear reactions depend heavily on the plasma environment [2]. Therefore, measurements of these reaction rates allow to draw conclusions about the plasma behavior.

In order for nuclear reactions to occur, the Coulomb barrier between the two reacting nuclei must be overcome. Even in stars, this is not classically possible: The thermal energy is much smaller than the energy necessary to combine two nuclei as close as the length scale of their nuclear radius. Instead, the cross section of the reaction, which is energy dependent, must be calculated quantum-mechanically because the ions still have a non-zero probability of presence in the "forbidden" region. This probability is highly dependent on the kinetic energy of the reacting ions relative to each other.

Because of the local charge separation in plasmas, the Coulomb potential can be quite strongly modified especially for larger distances, depending on the plasma parameters. This is the *plasma screening effect* which enhances the reaction rates in a plasma environment by reducing the Coulomb barrier. As detailed in Ref. [3], the bare cross-sections can be measured using neutral atoms and molecules, but taking into account another type of screening, *electron screening*, which is very distinct from the plasma screening considered here. In Ref. [4], this extraction of the bare cross-sections for laboratory measurements is discussed.

To calculate the *plasma screening factor*, the factor by which the reacting rates are enhanced, different models can be used. Historically, the weak screening model by Salpeter [2] serves as basis to several other models. As mentioned there, it is mathematically equivalent to the Debye-Hückel model for solutions of electrolytes [5]. Mitler improved this model using a more realistic approximation for the electron density and the *interaction energy* between two reacting ions [6]. His work is based on Ref. [7] and Ref. [8], where the approach by Salpeter [2] is extended. Refs. [6, 9] develop a different approach that uses the same electrostatic potential, but calculates the *penetrability* explicitly and the reaction rate is compared to a pure Coulomb potential. These three models are all classical or semiclassical. Alternatively, Ref. [10] uses the density matrix formalism to consider quantum mechanical effects. Other attempts to extend the weak screening are reviewed in Ref. [9], but are not discussed here.

Obtaining experimental data to test the validity of plasma screening models is difficult, because achieving in the laboratory the conditions under which plasma screening occurs is very challenging. So far, different screening models were only studied on the basis of reactions rates in astrophysical environments, which may be measured indirectly through astrophysical observations such as solar neutrino fluxes. In Ref. [9], such a comparison is performed, revealing a large discrepancy between the semiclassical theoretical models and the neutrino measurements. Using the quantum model [10], this discrepancy can be slightly reduced, but not removed. Ref. [4] explains that the actual discrepancy is mostly due to the phenomenon of neutrino oscillations reported in [11] (Super-Kamiokande) and [12] (Sudbury Neutrino Observatory) and is therefore not related to the used plasma models. Thus, the neutrino flux measurements do not yield precise enough values to decide which model is most appropriate for plasma screening [4]. Direct measurements of the plasma screening factor in plasma environments would be required for that.

As proposed in Ref. [13], colliding laser-produced plasmas can be used to investigate nuclear fusion in a plasma environment inside a laboratory. Solely heating a non-ionized gas in order to ionize it is rather impractical in a laboratory because of the high temperature required. Applying a strong electric field is much easier, but still the plasma conditions that could be achieved are far from those of astrophysical plasmas, hence the need for laser-generated plasmas. Several facilities exist today where strong enough optical lasers are available or being built [14–20]. One proposed setup discussed in the following requires two high-power optical lasers. Such lasers with a peak power up to 10 petawatt (PW) are being built at the Nuclear Pillar of the Extreme Light Infrastructure (ELI-NP) [21]. The experimental setup consists of a gas jet of helium or deuterium and

a solid target shown in Fig. 1.1. The gas jet is ionized by one laser pulse, while the other laser ionizes the solid target and accelerates this primary plasma towards the secondary helium or deuterium plasma. This setup would allow a measurement of plasma screened reaction rates in a laboratory, and the comparison of the measured screening effect to theoretical models.

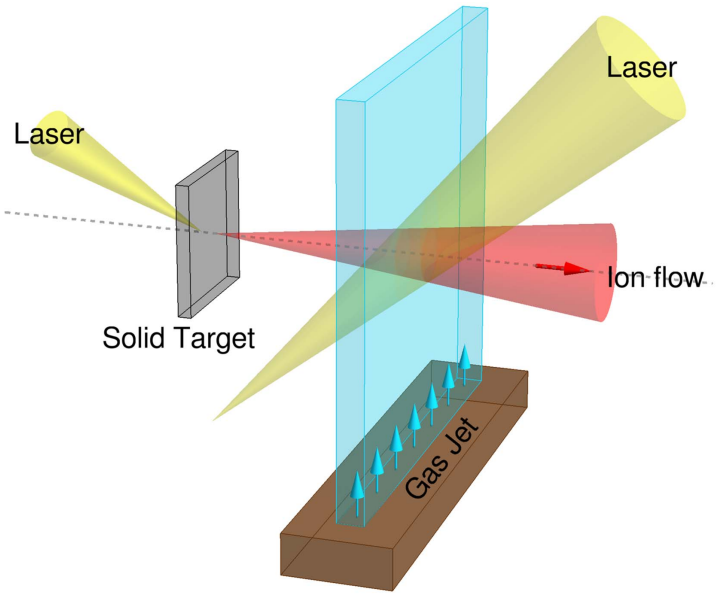

Figure 1.1: Experimental setup at ELI-NP, reproduced from Ref. [3].

In this work we perform for the first time calculations for the PW laser scenario taking into account the plasma screening effects based on several theoretical models. We use four plasma models: the Salpeter model [2], in the following denoted by M1, the Mitler model [6] (M2), a variant of M2 using the Wentzel–Kramers–Brillouin (WKB) method [6, 9] (M3), and the quantum mechanical model [10] (M4). Numerical results for these four models are presented for two reaction of astrophysical interest: $^{13}\mathrm{C}(\alpha,\mathrm{n})\,^{16}\mathrm{O}$, which is one of the important helium burning processes in advanced stellar phases as well as one of the interesting neutron sources for the slow neutron caption process of nucleosynthesis, and $^{7}\mathrm{Li}(\mathrm{d},\alpha)\alpha$, which might be the key to explain the lithium production problem of the standard big bang nucleosynthesis. We consider plasma densities in the region 10^{18}–10^{24} cm^{-3} and temperatures in the interval 50–100 eV for the respective applicability domain. Our results show that there are considerable differences between M1 and M2. M3 however does not differ significantly from M2 for all considered cases, a conclusion also noted in Ref. [9]. M4 differs from the other models slightly, but more so than M1, M2 and M3 among themselves especially at large temperatures and small R_D. For small

temperatures and large densities however, M4 is no longer applicable. Numerically, this conincides with severe difficulties with the used grid size and spacing. To verify the validity of the considered four models, the values computed here need to be compared to experimental data. We anticipate that a future experiment at ELI-NP as described above can yield precise enough measurements to enable this comparison.

This work is structured as follows: In Ch. 2, reaction rates and plasma screening are discussed. The relevant parameters and assumptions for all models are defined here. Ch. 3 discusses the classical and semiclassical models, M1, M2 and M3 in detail, i.e. their assumptions and derivation. In Ch. 4, M4 is described in great detail. The first part of Ch. 4 deals with the influence of the electrostatic energy on the screening factor, while the second part shows the calculation of the quantum mechanical deviation of the mean kinetic energy from the prediction of the equipartition theorem, $(3/2)k_{\mathrm{B}}T$. Ch. 5 shows the numerical results for the previously mentioned parameters. The work concludes with a summary and outlook in Ch. 6.

As unit system, (Hartree) atomic units are used throughout this work (unless otherwise mentioned), except for the temperatures and densities, which are given in eV and cm^{-3}.

2 Screening of reaction rates in a plasma

The plasma considered here is electrically neutral and consists of positive ions and electrons. It is large enough that boundary effects are negligible, and the time scale of the nuclear reactions is much smaller compared to any change in external parameters, which therefore can be considered as fixed. In the plasma environment, the other ions and electrons in the plasma affect the reacting ions. The classical model of Salpeter in Ref. [2] describes this *plasma screening* of the positive ions' pure Coulomb potential through "charge clouds", which reduce the Coulomb potential. Because these "charge clouds" are mostly determined by electrons, the electromagnetic field around the reaction ions can be treated electrostatically. This means that the reactions in the plasma can be considered quasi-static and statistical equilibrium is assumed at all times.

2.1 Reaction rates

For a reaction between two ions to occur, they first have to overcome the Coulomb barrier. Because the Coulomb potential is screened by the plasma environment, there is an increased reaction rate compared to a pure Coulomb potential. Since the cross section is highly dependent on the kinetic energy, the reaction rates can be calculated by integrating the cross section over all possible energies weighted with the kinetic energy distribution of the reacting ions in the plasma. For the cases considered here, a classical Maxwell-Boltzmann distribution is used. The intrinsic nuclear part S of the cross section $\sigma(E) =: P(E)S/E$ with penetrability $P(E)$ is considered to be negligibly dependent on the kinetic energy of the reacting ions [9].

Let $v(E) \approx \sqrt{2E/m_{\mathrm{red}}}$ be the non-relativistic velocity of the reacting ions with m_{red} being their reduced mass, and E their relative kinetic energy. Given the cross section $\sigma(E)$ of the reaction in question, the unscreened, average reaction rate per volume and per number density of both reactants for a Maxwell-Boltzmann distribution at

temperature T is

$$\langle \sigma v \rangle = \frac{2\beta^{\frac{3}{2}}}{\sqrt{\pi}} \int_0^\infty dE \sigma(E) v(E) \sqrt{E} e^{-\beta E}, \tag{2.1}$$

see Ref. [2], Eq. (1) or Ref. [9], Eq. (6). $\beta := 1/(k_\mathrm{B}T)$ is the thermodynamic beta. In Eq. (2.1), the integrand is almost zero except for a small region around the *Gamow energy* [6]. Here, the "joint probability" for the relative kinetic energy to occur in the Maxwell-Boltzmann distribution and for the tunneling to be "successful" is maximal. For a pure Coulomb potential between ions with charge numbers Z_1 and Z_2, the Gamow peak of the integrand is at

$$E_{\mathrm{G,\ pure}} = \left(\frac{1}{\beta} \sqrt{\frac{m_\mathrm{red}}{2}} Z_1 Z_2 \right)^{\frac{2}{3}}; \tag{2.2}$$

for the derivation see Eq. (3.44).

2.2 Screening factor

The temperature is assumed to be low enough such that the classical turning point between the ions is much larger than the length scale on which nuclear reactions take place. Therefore, the influences of nuclear and plasma effects are well separated, meaning that the intrinsic nuclear part of the cross-section is assumed to be constant. This is done by calculating an enhancement factor, i.e., the ratio of the reaction rate in the considered plasma and the theoretical reaction rate calculated by considering a pure Coulomb potential. If the separation of nuclear and plasma effects is assumed, it can be seen that for a wide range of parameters, the screening factor can be calculated without an integration over the cross section and is not significantly dependent on the masses of the reacting nuclei. Therefore, this enhancement factor f is precisely what we want to calculate in order to be able to compare the plasma screening model to experimental measurements:

$$f := \frac{\langle \sigma v \rangle_\mathrm{screened}}{\langle \sigma v \rangle_\mathrm{unscreened}} \tag{2.3}$$

2.3 Plasma parameters

The relevant parameters used are the temperature T (or β), as well as the charge, mass and densities of the plasma constituents and the reacting ions. Let Z_i be the charge number of the ion with index i, A_i its mass number and X_i its mass fraction in the plasma. Given the mass density ρ_{mass}, the baryon number density n_{ba} and the electron number density n_{e} are (neglecting the electron mass)

$$n_{\mathrm{ba}} = \frac{1}{\mathrm{u}}\rho_{\mathrm{mass}}, \tag{2.4}$$

$$n_{\mathrm{e}} = n_{\mathrm{ba}} \sum_i \frac{Z_i X_i}{A_i}, \tag{2.5}$$

with the atomic mass unit u.

In the following, the indices 1 and 2 stand for the considered reacting ions, with $Z_1 \geq Z_2$. X_1 and X_2 may be negligible, e.g. when the reacting ions are not part of the plasma, but are introduced externally as an ion beam. Their kinetic energy is still assumed to be thermal.

Because statistical equilibrium is assumed, the electron and ion densities are modified by a Boltzmann factor:

$$n_i(\vec{r}) = \bar{n}_i e^{-\beta Z_i e \Phi_Z(\vec{r})}, \tag{2.6}$$

$$n_{\mathrm{e}}(\vec{r}) = \bar{n}_{\mathrm{e}} e^{\beta e \Phi_Z(\vec{r})}, \tag{2.7}$$

where the sum over i is taken over all significantly abundant ions in the plasma. Furthermore, $\Phi_Z(\vec{r})$ is the spatially dependent electrostatic potential around an ion (or two "combined" ions) with charge Z, which is spherically symmetric because of the assumption of a homogeneous plasma. The potential is given by the Poisson-Boltzmann equation — Ref. [2], Eq. (15) and Eq. (16):

$$\vec{\nabla}^2 \Phi_Z(\vec{r}) = -4\pi \left(Z\delta^{(3)}(\vec{r}) + n_{\mathrm{ba}} \sum_i \frac{Z_i X_i}{A_i} e^{-\beta Z_i \Phi_Z(\vec{r})} - n_{\mathrm{e}} e^{\beta \Phi_Z(\vec{r})} \right). \tag{2.8}$$

(See Sec. 2.3 for the parameters.)

These assumptions are shared by all models treated here, with the exception of the electron density in Eq. (2.8), which is calculated differently in the quantum mechanical model described in Sec. 4.1.

In the next chapters, we proceed to introduce these models in more detail. M1, M2

and M3, the classical and semiclassical models, are described in Ch. 3, whereas M4 is reviewed in Ch. 4.

3 Classical and semiclassical models

The first model described here is the weak screening model (M1) developed by Salpeter in Ref. [2], which is (apart from the electron degeneracy factor) purely classical. It also forms the basis for all other discussed models. The used linear approximation of the Poisson-Boltzmann equation, Eq. (3.1) results in the Debye-Hückel potential.

To improve this model considerably, the electrostatic potential was more carefully derived by Mitler in Ref. [6] to obtain a better behavior at the origin (M2). Instead of using the potential energy directly as interaction energy, the change in free energy when combining the reacting ions is used.

In the model of Ref. [9] (M3), the ratio of the screened and unscreened reaction rates are calculated directly. For this, the WKB approximation is chosen instead of the "amplitude density function" method in the paper. The quantum mechanical effects are instead considered more elaborately in the dedicated quantum mechanical model (M4) in the next chapter.

3.1 Salpeter's model for weak screening (M1)

3.1.1 Assumptions

Let $a = \sqrt[3]{1/(4\pi n_{\mathrm{ba}})}$. Then inside a sphere of radius a, a mass of $\frac{1}{3}$u (atomic mass unit) is contained. The assumption of statistical equilibrium is valid if a is small compared to the characteristic scale of the charge distribution, the Debye-Hückel radius R_{D} (Eq. (3.5)). This is fulfilled for low densities and high temperatures. To justify the linear approximation in the Poisson-Boltzmann equation in Eq. (3.1), the Coulomb energy between Z_1 and Z_2 should be small compared to β^{-1}. As noted in Ref. [9], this is given for $R_{\mathrm{D}} \gg r_{\mathrm{t}}$ with the classical turning point of the potential energy for the ion Z_i, r_{t}. The semi-classical treatment of the electrons is valid if the (absolute value of the) energy of the bound states is much smaller than the thermal energy. For a ground-state electron (first quantum number $n = 1$) in a hydrogen-like atom of charge Z, this

means $\beta Z^2/2 \ll 1$. This condition is not fulfilled for the lowest temperatures considered in Ch. 5, especially with ions of high charge numbers. At higher temperatures, this problem does not appear. These assumptions are described in more detail in Ref. [2].

In addition, the weak screening model accounts for the statistical nature of the electrons with a modified $\tilde{R}_\mathrm{D}$, as described in Sec. 3.1.3.

3.1.2 Derivation

In the considered scenario, Z_1 is fixed at the origin and the effect of the electrostatic potential on Z_2 are regarded. This assumption is only symmetric in Z_1 and Z_2 for the model discussed here; in the Mitler model, the change in free energy when combining Z_1 and Z_2 is calculated from the electrostatic energy, and in the WKB model, the calculation is done in the center of mass frame using the reduced mass. To solve the Poisson-Boltzmann equation (2.8) analytically, the exponentials are approximated to linear order:

$$\vec{\nabla}^2\Phi(\vec{r}) = 4\pi\left(-Z_1\delta^{(3)}(\vec{r}) + n_\mathrm{ba}\sum_i \frac{Z_i X_i}{A_i}\beta Z_i\Phi(\vec{r}) + n_\mathrm{e}\beta\Phi(\vec{r})\right). \tag{3.1}$$

The constant terms of the expansions cancel each other due to Eq. (2.5). Because the problem is spherically symmetric (in the Z_1 coordinate system) and as per assumption electrostatic, this is an inhomogeneous ordinary differential equation of second order in r. With $\Psi(r) \coloneqq \Phi(r) - Z_1/r$, it becomes

$$\left(\frac{2}{r}\frac{\partial}{\partial r} + \frac{\partial^2}{\partial r^2}\right)\Psi(r) = 4\pi\left(n_\mathrm{ba}\sum_i \frac{Z_i X_i}{A_i}\beta Z_i + n_\mathrm{e}\beta\right)\left(\frac{Z_1}{r} + \Psi(r)\right). \tag{3.2}$$

The homogeneous equation without the $1/r$-term is solved by the following two solutions:

$$\tilde{\Psi}_1(r) = \frac{Z_1}{r}e^{-\frac{r}{R_\mathrm{D}}}, \tag{3.3}$$

$$\tilde{\Psi}_2(r) = \frac{Z_1}{r}e^{\frac{r}{R_\mathrm{D}}}. \tag{3.4}$$

There, R_D is the Debye-Hückel radius, given by

$${R_\mathrm{D}}^{-2} = 4\pi\left(n_\mathrm{ba}\sum_i \frac{Z_i X_i}{A_i}\beta Z_i + n_\mathrm{e}\beta\right) = 4\pi n_\mathrm{ba}\beta\sum_i \frac{X_i}{A_i}\left(Z_i^2 + Z_i\right). \tag{3.5}$$

The two solutions $\tilde{\Psi}_1$ and $\tilde{\Psi}_2$ are linearly independent, because the Wronskian is

$$\tilde{\Psi}_1\tilde{\Psi}_2' - \tilde{\Psi}_2\tilde{\Psi}_1' = -\frac{2Z_1^2}{r^2 R_\mathrm{D}} \not\equiv 0. \tag{3.6}$$

A particular solution of the inhomogeneous equation is given by

$$\Psi = \frac{Z_1}{r}\left(e^{-\frac{r}{R_\mathrm{D}}} - 1\right). \tag{3.7}$$

Because $\lim_{r\to\infty} \tilde{\Psi}_2(r) = \infty$, and Φ should go to Z_1/r (plus a constant term) for $r \to 0$, this particular solution is already the only physical solution.

The effect of Ψ is to increase the kinetic energy of the other reacting particle Z_1 compared to a pure Coulomb potential because of the increased potential energy ("interaction energy")

$$\delta V(r) = Z_2\Psi(r) \approx \delta V(0) = \frac{Z_1 Z_2}{R_\mathrm{D}}. \tag{3.8}$$

Modifying Eq. (2.1) with this shift gives then

$$\langle\sigma v\rangle_\mathrm{screened} = \frac{2\beta^{\frac{3}{2}}}{\sqrt{\pi}} \int_{\delta V(0)}^{\infty} dE'\sigma(E')v(E)\sqrt{E}e^{-\beta E} \tag{3.9}$$

as described in Ref. [9]. The kinetic energy is shifted by $E \to E' = E + \delta V(0)$.

Due to the assumption that the classical turning point is much smaller than R_D, we have $V(0) \ll E_{\mathrm{G,\,pure}}$ with the Gamow energy $E_{\mathrm{G,\,pure}}$ from Eq. (3.44), and thus the screened reacting rate becomes

$$\langle\sigma v\rangle_\mathrm{screened} = \frac{2\beta^{\frac{3}{2}}}{\sqrt{\pi}} \int_{0}^{\infty} dE'\sigma(E')v(E')\sqrt{E'}e^{-\beta(E'-\delta V(0))}. \tag{3.10}$$

The screened rate therefore differs from the unscreened rate only by the enhancement factor [see Eq. (2.3)]

$$f = e^{\beta\delta V(0)}. \tag{3.11}$$

3.1.3 Electron degeneracy

In the model of Ref. [2], the only non-classical consideration is a change of R_D by considering the Fermi-Dirac statistics for the electrons, which are treated as a Fermi

gas. For low enough densities (see Sec. 3.1.1), the ratio of the Fermi energy to the thermal energy $k_\mathrm{B}T$ is given by

$$D \coloneqq \beta E_\mathrm{F} = \beta \frac{1}{2} (3\pi^2 n_\mathrm{e})^{\frac{2}{3}}. \tag{3.12}$$

For a free Fermi gas, the mean electron density can be calculated as

$$n_\mathrm{e} = \frac{\sqrt{2}}{\pi^2} \beta^{\frac{2}{3}} f(\eta) \tag{3.13}$$

with the Fermi-Dirac integral

$$f(\eta) = \int_0^\infty dx \frac{\sqrt{x}}{e^{(x-\eta)} + 1} \tag{3.14}$$

and $\eta = \beta\mu$, where μ is the chemical potential. This way, η can be determined by solving Eq. (3.13) numerically. Given the (change in) potential energy for the electrons, $V_\mathrm{e} = -e\Psi$, the electron density is given by

$$n_\mathrm{e} \frac{f(\eta - \beta V_\mathrm{e}(r))}{f(\eta)} \approx 1 - \beta V_\mathrm{e}(r) \frac{f'(\eta)}{f(\eta)}$$

instead of the Boltzmann factor. This means that the Debye-Hückel radius is replaced for all calculations by

$$\tilde{R}_\mathrm{D}^{-2} = 4\pi n_\mathrm{ba} \beta \sum_i \frac{X_i}{A_i} \left(Z_i^2 + Z_i \frac{f'(\eta)}{f(\eta)} \right). \tag{3.15}$$

For this model, this means replacing R_D by $\tilde{R}_\mathrm{D}$ in Eq. (3.8) and correspondingly in Eq. (3.11).

3.1.4 Summary

Because of the rather strong assumptions used in this model, the calculation of the screening factor is very easy. Given $\tilde{R}_\mathrm{D}$ from Eq. (3.15), or only R_D with $f'/f \approx 1$, the screening factor f is obtained from Eq. (3.11) with Eq. (3.8).

3.2 Mitler formula (M2)

The model discussed next is the first part of "Model A" by Mitler in Ref. [6].

3.2.1 Derivation

Potential

To calculate the change in free energy (in Sec. 3.2.1), the potential is not only calculated for a charge Z_1 as in the weak screening model, but for an arbitrary charge Z. The Poisson-Boltzmann equation, Eq. (2.8), is still used. However, it is not linearly approximated as before, but only for large r. This is performed by splitting the density into two parts: $r < r_1$ and $r > r_1$, where r_1 is determined in order to fulfill correct normalization (i.e. a total charge of 0). For small r, the electron density is approximated by the constant plasma mean density n_e, unlike for the Debye-Hückel result, where it diverges. For large r, the previous solution for the linear approximation of the Poisson-Boltzmann is still used, with $\tilde{R}_\mathrm{D}$ from Eq. (3.15). The result is:

$$\rho_Z(r) = \begin{cases} \rho_{Z,\mathrm{inside}}(r) \approx Z\delta^{(3)}(r) - n_\mathrm{e}, & r < r_1, \\ \rho_{Z,\mathrm{outside}}(r) \approx -r_1 n_\mathrm{e} \dfrac{e^{-\tilde{R}_\mathrm{D}^{-1}(r-r_1)}}{r}, & r > r_1, \end{cases} \tag{3.16}$$

$$\text{with } r_1 = \tilde{R}_\mathrm{D} \left(\frac{3Z}{4\pi n_\mathrm{e} \tilde{R}_\mathrm{D}^3} + 1 \right)^{\frac{1}{3}} - \tilde{R}_\mathrm{D} \tag{3.17}$$

With the normalization constant of $\rho_{Z,\mathrm{outside}}$ defined in this manner, ρ_Z is automatically continuous at $r = r_1$. r_1 can be calculated by solving $\int d^3r \rho_Z(\vec{r}) \stackrel{!}{=} 0$, for which there only is one real solution. The potential is then simply given by solving the Poisson equation $\vec{\nabla}^2 \Phi_Z = -4\pi\rho_Z$ analytically:

$$\Phi_Z(r) = \begin{cases} \dfrac{Z}{r} - 2\pi n_\mathrm{e}(2\tilde{R}_\mathrm{D} r_1 + r_1^2) + \dfrac{2}{3}\pi n_\mathrm{e} r^2, & r < r_1, \\ 4\pi n_\mathrm{e} r_1 \tilde{R}_\mathrm{D}^2 \dfrac{e^{-\tilde{R}_\mathrm{D}^{-1}(r-r_1)}}{r}, & r > r_1. \end{cases} \tag{3.18}$$

The solution for $r < r_1$ is unique, because the (non-constant) homogeneous solution of the radial Laplace equation for $r > 0$, $\propto 1/r$, is fixed by the delta function of $\rho_{Z,\mathrm{inside}}$. The constant term is chosen to ensure Φ_Z is continuous at $r = r_1$. For $r > r_1$, the solution is unique, because the the potential should go to 0 for $r \to \infty$, which implies a vanishing constant term. Including a term $\propto 1/r$ would make the r-derivative at $r = r_1$

discontinuous. For weak screening with strong non-degeneracy, $\tilde{R}_\mathrm{D} \approx R_\mathrm{D}$ and $r_1 \approx 0$, from which the previous result, the Debye-Hückel potential, is recovered.

Free energy

The potential energy $Z_2\Phi_{Z_1}$ is not symmetric in 1 and 2, because the respective "polarization clouds" do not superimpose linearly, but continuously deform. To account for this, the interaction energy is rather taken to be the change in free (Helmholtz) energy $\Delta F(r)$, with r being the distance between Z_1 and Z_2.

Thus Eq. (3.8) is, to first order, replaced by

$$V(r) \approx \frac{Z_1 Z_2 e^2}{r} + \Delta F(0), \tag{3.19}$$

with the change in free energy when "combining" Z_1 and Z_2, $\Delta F(0) = \Delta F(r = 0)$. In order to determine $\Delta F(0)$, the work done by combining Z_1 and Z_2 needs to be calculated from the change in electrostatic self-energy. The latter, excluding the infinite self-energy of the charge Z, is given by

$$U_Z = \frac{Z}{2}\delta\Phi_Z(0) + \frac{1}{2}\int d^3r \Phi_Z(r)\delta\rho_Z(r) \tag{3.20}$$

with $\delta\Phi_Z = \Phi - \frac{Z}{r}$ and $\delta\rho = \rho - Z\delta^{(3)}(r)$, as stated in Ref. [10]. For the previously calculated charge density and potential, Eq. (3.16) and Eq. (3.18), respectively, the electrostatic energy is given by

$$U_Z = 2\pi n_\mathrm{e} r_1 \left(-2\pi\tilde{R}_\mathrm{D}^3 n_\mathrm{e} r_1 - \tilde{R}_\mathrm{D} Z + \frac{4}{3}\pi\tilde{R}_\mathrm{D} n_\mathrm{e} r_1^3 - Z r_1 + \frac{8}{15}\pi n_\mathrm{e} r_1^4 \right). \tag{3.21}$$

To obtain the free energy, we consider the canonical partition function Z_part. The free energy and the mean energy (ensemble average) are given by

$$\langle U(\beta)\rangle = -\frac{\partial}{\partial\beta}\ln(Z_\mathrm{part}), \tag{3.22}$$

$$F = -\frac{1}{\beta}\ln(Z_\mathrm{part}). \tag{3.23}$$

We then obtain:

$$\frac{\partial}{\partial\beta}(\beta F) = \langle U(\beta)\rangle \qquad \text{and} \tag{3.24}$$

$$\beta F\Big|_{\beta=0} = 0 \tag{3.25}$$

$$\implies \beta F = \int_0^\beta \langle U(\tau)\rangle \, d\tau. \tag{3.26}$$

Setting $\langle U\rangle = U_Z$ and integrating over $a \coloneqq 1/\tilde{R}_\mathrm{D}^3$, this results in the free energy

$$F_Z = \frac{2}{3}\frac{1}{a^{\frac{2}{3}}}\int_0^a U_Z(a')\, da \tag{3.27}$$

$$= -\frac{8}{5}\pi^2 n_\mathrm{e}^2 \tilde{R}_\mathrm{D}^5 \left[\left(1 + \frac{3Z}{4\pi\tilde{R}_\mathrm{D}^3 n_\mathrm{e}}\right)^{\frac{5}{3}} - 1 - \frac{5Z}{4\pi\tilde{R}_\mathrm{D}^3 n_\mathrm{e}}\right] \tag{3.28}$$

$$= -\frac{8}{5}\pi^2 n_\mathrm{e}^2 \tilde{R}_\mathrm{D}^5 \left((\zeta_Z + 1)^{\frac{5}{3}} - 1 - \frac{5}{3}\zeta_Z\right), \tag{3.29}$$

where $\zeta_Z = 3Z/(4\pi n_\mathrm{e}\tilde{R}_\mathrm{D}^3)$. Thus the difference in free energy when combining Z_1 and Z_2 from being infinitely far separated is

$$\begin{aligned}\Delta F(0) &= F_{Z_1+Z_2} - F_{Z_1} - F_{Z_2} \\ &= -\frac{8}{5}\pi^2 n_\mathrm{e}^2 \tilde{R}_\mathrm{D}^5 \left((\zeta_{Z_1} + \zeta_{Z_2} + 1)^{\frac{5}{3}} - (\zeta_{Z_1} + 1)^{\frac{5}{3}} - (\zeta_{Z_2} + 1)^{\frac{5}{3}} + 1\right).\end{aligned} \tag{3.30}$$

If Eq. (3.11) is still assumed, the enhancement factor becomes

$$f = e^{\beta|\Delta F(0)|}. \tag{3.31}$$

As noted by Mitler, the linear approximation which leads to Eq. (3.11) increases the inaccuracy of the linear approximation of the Poisson-Boltzmann equation for plasma parameters where the linearization it is no longer valid. Instead, the screened and unscreened reaction rates should be calculated more accurately, e.g. with the WKB approximation for the penetration factor, as discussed in the next section.

3.3 WKB method (M3)

Instead of using Eq. (3.31), the reaction rates with and without screening are calculated and then compared. This is described in Ref. [9].

3.3.1 WKB wave function in a temporally constant potential

This section follows the derivation of the one-dimensional WKB wave function of a single particle in a slowly varying potential from Ref. [22], section 31.3, generalized to 3 dimension with spherical symmetry. $\hbar$, which is 1 in atomic units, is restored only in this section to separate the order of the derivatives. Assuming $V(r) \geq E$, the radial wave function of a single particle can be calculated. The Schrödinger equation (with $\hbar$ restored) for a particle with mass m is

$$-\frac{\hbar^2}{2m}\vec{\nabla}^2\Psi(r) = (E - V(r))\Psi(r) \tag{3.32}$$

with constant total energy E and potential $V(r)$. Using $\Psi(r) = \Psi_0 e^{-f(r)/\hbar}$ with a real function f in Eq. (3.32), this results in

$$-\frac{\hbar^2}{2m}\vec{\nabla}^2 e^{-\frac{f(r)}{\hbar}} = (E - V(r))e^{-\frac{f(r)}{\hbar}} \tag{3.33}$$

$$\implies \hbar\vec{\nabla}^2 f - \left(\vec{\nabla} f\right)^2 = 2m(E - V(r)) \tag{3.34}$$

$$\implies \left(\vec{\nabla} f\right)^2 - \hbar\vec{\nabla}^2 f = 2m(V(r) - E). \tag{3.35}$$

Using the WKB idea of separating the partial differential equation in orders of $\hbar$, which correspond to the orders of the derivatives, we can write $f = W + \hbar W_1 + \cdots$. The differential equation Eq. (3.35) is fulfilled for W approximately by using only the parts with power $\hbar^0$:

$$\implies \left(\vec{\nabla} W\right)^2 = 2m(V(r) - E) \tag{3.36}$$

i.e. (only using the radial part)

$$\left(\frac{df}{dr}\right)^2 = 2m(V(r) - E). \tag{3.37}$$

To compute the penetration factor, the probability density at $r = 0$ compared to the classical turning point r_t with $E = V(r_\mathrm{t})$ is determined. Thus

$$W(r) = \pm \int_r^{r_\mathrm{t}} dr' \sqrt{2m(V(r') - E)}. \tag{3.38}$$

Only the positive solution makes sense, because the probability should fall for small r and not rise exponentially. This approximation is valid for small wavelengths, that is for $\hbar^{-1}\sqrt{2m(V-E)} \gg r_\mathrm{t}$.

We now turn to the calculation of the screening factor using the results from this section.

3.3.2 Derivation

The reaction rates are calculated from Eq. (2.1) for an unscreened $\sigma_\mathrm{unscreened}(E)$ and a screened $\sigma_\mathrm{screened}(E)$. The cross section can be written as

$$\sigma(E) = \frac{S(E)}{E} P(E) \tag{3.39}$$

with nuclear part $S(E) \approx S$, which is approximately constant. $P(E)$ is the penetration factor, which can be obtained from the electrostatic potential. For this the WKB approximation is used. From the preceding paragraph, the penetration factor can be obtained from

$$P(E) =: e^{-G(E)} = \frac{|\Psi(0)|^2}{|\Psi(r_\mathrm{t})|^2} = e^{-2W(0)} \tag{3.40}$$

$$= \exp\left(-2\sqrt{2\mu} \int_0^{r_\mathrm{t}} dr' \sqrt{V(r') - E} \right) \tag{3.41}$$

where m was substituted by the reduced mass μ of the reacting ions and $\hbar = 1$ was omitted again.

For a pure Coulomb potential, $V = Z_1 Z_2 / r$, $G(E)$ can be obtained analytically:

$$G(E) = 2\sqrt{2\mu} \int_0^{\frac{Z_1 Z_2}{E}} dr' \sqrt{\frac{Z_1 Z_2}{r'} - E} = \frac{\sqrt{2\mu}\pi Z_1 Z_2}{\sqrt{E}}. \tag{3.42}$$

To obtain $G(E)$ for the screened potential, the integration needs to be performed nu-

merically. With the electrostatic potential $\Phi_Z(r)$ from Eq. (3.18), the potential is given by $V(r) = Z_1\Phi_{Z_2}(r) \equiv Z_2\Phi_{Z_1}(r)$.

3.3.3 Gamow energy

As mentioned in 3.1.2, the factor $\exp(-G(E) - \beta E)$ almost vanishes everywhere except for a small region around the Gamow energy $E_\mathrm{G} > 0$, at which it is maximal. To find the Gamow energy, $G(E) + \beta E$ needs to be minimized. Because the second derivative of this expression is positive,

$$G'(E_\mathrm{G}) + \beta \stackrel{!}{=} 0 \tag{3.43}$$

$$\Longrightarrow E_\mathrm{G} = \left(\sqrt{\frac{\mu}{2}}\pi Z_1 Z_2 \beta\right)^{\frac{2}{3}} \tag{3.44}$$

for a pure Coulomb potential.

3.3.4 Numerical calculation

We are only interested in the ratio of the screened and unscreened reaction rates, not their absolute values. Thus it is advantageous to calculate values proportional to the rates which are not too small to handle numerically with a (double-precision) floating point representation. To achieve this, the factor $\exp\left(-G(E) - \beta E\right)$ is replaced by $\exp\left(-G(E) - \beta E + G(E_{\mathrm{G,pure}}) + E_{\mathrm{G,pure}}\right)$ with the Gamow energy for the pure Coulomb potential, $E_{\mathrm{G,pure}}$, from Eq. (3.44) for both reaction rates. Doing so prevents rounding the exponential to 0.

4 Quantum model (M4)

This model from Ref. [10] (M4) also calculates the change in free energy for the screening factor in Eq. (3.31), as does the Mitler model M2. However, the electrons are treated much more extensively via the density matrix formalism described in Ref. [23]. In the first part, the change in free energy is determined by numerically calculating the diagonal of the density matrix, which is proportional to the electron density. Using this electron density, the Poisson-Boltzmann equation is solved numerically to obtain the potential and finally the electrostatic energy.
For the second part, the assumption that the electrons have a mean kinetic energy of $(3/2)k_{\mathrm{B}}T$ is dropped and the corresponding change in free energy calculated from the density matrix for the electrons. The Debye-Hückel potential is used for large r, and for small r the density matrix is obtained from bound and continuum eigenstates with corresponding Boltzmann factors.
Both parts are only valid as long as $\beta/\tilde{R}_{\mathrm{D}}$ is small enough. This is due to the used approximations of the potential and charge density by the Debye-Hückel potential, which is not valid if $\beta > \tilde{R}_{\mathrm{D}}$. In the first part, this could be alleviated by using the Mitler potential instead as initial value and for large r, but this is out of scope for this work.

4.1 Density matrix formalism

4.1.1 Derivation

Density matrix in the canonical ensemble

The density operator is defined as

$$\hat{\rho} = p_i \sum_i |\psi_i\rangle \langle\psi_i| \tag{4.1}$$

for a normalized basis ψ_i of the Hilbert space and probabilities p_i. In position representation, the density "matrix" is defined as

$$\rho(\vec{x}, \vec{x}') = \langle \vec{x} | \, \hat{\rho} \, | \vec{x}' \rangle \, . \tag{4.2}$$

The "diagonal" of the density matrix is the probability density:

$$\rho(\vec{x}) = \rho(\vec{x}, \vec{x}). \tag{4.3}$$

In the canonical ensemble in statistical equilibrium, the density operator is given by

$$\hat{\rho} = e^{\beta F} e^{-\beta \hat{H}} \tag{4.4}$$

with normalization $\exp(\beta F) \coloneqq \mathrm{Tr}[\exp(-\beta \hat{H})]$. This is described in Chapter 2.3 of Ref. [23]. $\hat{H} = -(1/2)\vec{\nabla}^2 + V$ is the Hamilton operator of the system with potential energy V and $\beta = 1/(k_\mathrm{B} T)$ with temperature T.

In the following, the factor $\exp(\beta F)$ is omitted and the unnormalized density matrix is used. To obtain the number density of the described particles, the result is divided by the corresponding value for a uniform distribution, i.e. with $V = 0$. Thus

$$-\frac{\partial}{\partial \beta} \hat{\rho} = \hat{H} \hat{\rho} \tag{4.5}$$

$$\implies -\frac{\partial}{\partial \beta} \langle \vec{x} | \, \hat{\rho} \, | \vec{x}' \rangle = \langle \vec{x} | \, \hat{H} \hat{\rho} \, | \vec{x}' \rangle \tag{4.6}$$

$$= \langle \hat{H} \vec{x} | \, \hat{\rho} \, | \vec{x}' \rangle \, , \tag{4.7}$$

because $\hat{H}$ is Hermitian. In position representation

$$\frac{\partial}{\partial \beta} \rho(\vec{x}, \vec{x}'; \beta) = \left(\frac{1}{2} \vec{\nabla}_x^2 - V(\vec{x}) \right) \rho(\vec{x}, \vec{x}'; \beta). \tag{4.8}$$

In the limit of infinite temperature, the unnormalized density operator is $\hat{\rho} = \mathbb{1}$, because $\beta = 0$. The initial condition for the partial differential equation (4.8) at $\beta = 0$ is thus

$$\rho(\vec{x}, \vec{x}'; 0) = \langle \vec{x} | \, \mathbb{1} \, | \vec{x}' \rangle = \delta^{(3)}(\vec{x} - \vec{x}'). \tag{4.9}$$

This implies a uniform distribution without any spatial correlation, as would be expected in the high-temperature limit. To obtain the density matrix at inverse temperature β,

Eq. (4.8) can be integrated from $\tilde{\beta} = 0$ to $\tilde{\beta} = \beta$. For $V = 0$, this results in

$$\rho_0(\vec{x}, \vec{x}'; \beta) = \left(\frac{m}{2\pi\beta}\right)^{\frac{3}{2}} e^{-\beta\frac{m}{2}|\vec{x}-x'|^2}. \tag{4.10}$$

The probability density is then

$$\rho_{\text{prob.}}(\vec{x}) = \frac{\rho(\vec{x}, \vec{x}; \beta)}{\rho_0(\vec{x}, \vec{x}; \beta)} = \left(\frac{2\pi\beta}{m}\right)^{\frac{3}{2}} \rho(\vec{x}, \vec{x}; \beta). \tag{4.11}$$

Total charge density

The charge density can be calculated given the electrostatic potential Φ_Z. For electrons, the potential energy is simply $V_Z = -\Phi_Z$. With the density matrix obtained from the preceding section with $V = V_Z$ and $m = 1$ (electron mass), the electron density is

$$n_{\text{e}}\rho_{\text{e}}(r) = n_{\text{e}}(2\pi\beta)^{\frac{3}{2}}\rho(\vec{r}, \vec{r}; \beta) \tag{4.12}$$

with the average plasma electron density n_{e}. The rest of the total charge density is the same as in Eq. (2.8):

$$\rho_{\text{total}} = Z\delta^{(3)}(\vec{r}) + n_{\text{ba}} \sum_i \frac{Z_i X_i}{A_i} e^{-\beta Z_i \Phi_Z(r)} - n_{\text{e}}\rho_{\text{e}}. \tag{4.13}$$

Potential

To obtain the potential, the Poisson-Boltzmann equation with the charge density from Eq. (4.13) is solved numerically. Instead of solving for the divergent Φ_Z, the equation is solved for $\delta\Phi_Z = \Phi_Z - Z/r$:

$$\vec{\nabla}^2 \delta\Phi_Z = -4\pi \left(n_{\text{ba}} \sum_i \frac{Z_i X_i}{A_i} e^{-\beta Z_i \left(\delta\Phi_Z(r) + \frac{Z}{r}\right)} - n_{\text{e}}\rho_{\text{e}} \right). \tag{4.14}$$

Screening factor

The electrostatic energy U_Z is calculated by iterating the above procedure three times. As starting potential, the Debye-Hückel potential

$$\Phi_Z(r) = \frac{Z}{r} \exp -\frac{r}{\tilde{R}_{\text{D}}} \tag{4.15}$$

is used and from this the electron density calculated with the density matrix formalism. The potential does not depend on the integration variable $\tilde{\beta}$, because the electron density is calculated for the (in the current iteration) given fixed potential. Solving Eq. (4.14) yields then the improved potential. U_Z can then be obtained from Eq. (3.20). To get the corresponding free energy, Eq. (3.26) is numerically integrated:

$$F_Z = \frac{1}{\beta} \int_0^\beta U_Z(\tau)\, d\tau. \tag{4.16}$$

Obviously, $\tilde{R}_\mathrm{D}$ is dependent on τ and must be calculated for each $U_Z(\tau)$. Eq. (3.31) is then used to calculate the enhancement factor, with

$$\Delta F(0) = F_{Z_1+Z_2} - F_{Z_1} - F_{Z_2}. \tag{4.17}$$

4.1.2 Numerical calculation

Eq. (4.8) and Eq. (4.14) are both solved numerically as described in the following.

Electron density

In order to solve the partial differential equation (4.14), space and the integration variable, now called τ, are discretized.

As described in Ref. [10], a 30^3 grid with 31^3 points and a spacing of $\Delta = 0.015$ are used. The Laplace operator is approximated by using central finite differences with a five-point stencil and propagating explicitly from $\tau = 0$ to $\tau = \beta$.

To obtain the density matrix for different $\vec{r}$, this integration needs to be performed for different $\vec{x}' = \vec{r}$. Due to the spherical symmetry and because the only point of interest is the diagonal $\vec{x} = \vec{x}'$, $\vec{x}' = 0$ can be chosen, but the potential shifted such that it is centered at $\vec{x}'$. The diagonal element is then the value at the origin for every $\vec{r}$. This guarantees that the point of interest is always in the middle of the grid and boundary effects are reduced. The term $1/r$ is regulated as described in Sec. 4.1.2.

The $\vec{r}$ points are chosen on a diagonal of the grid from $r = 0$ to $r \approx r_\mathrm{max} = 0.4 \lessapprox \tilde{R}_\mathrm{D}$. Φ_Z is given for discrete (one-dimensional) $r = 0$ until $r = r_\mathrm{max}$, which is detailed in the next section. For $r \leq r_\mathrm{max}$, Φ_Z is interpolated using a cubic spline, while for $r > r_\mathrm{max}$, the classical Debye-Hückel potential, $V = -Z/r \exp(-r/\tilde{R}_\mathrm{D})$, is used.

Because the initial condition is a δ-function, which can not be (directly) used numer-

ically, an approximation needs to be used. For this, the analytical solution Eq. (4.10) is used at $\tau = \tau_0$, essentially neglecting the potential at high temperatures. The numerical integration with the potential is then continued from $\tau = \tau_0$ to $\tau = \beta$. In order to determine a good τ_0, the steps in Ref. [24], page 2213, are used for the chosen grid spacing Δ and the "support" $r_{\max}$. This means solving the equation

$$\exp\left(x^2 - \frac{\pi^2 m^2}{x^2}\right) \stackrel{!}{=} \frac{m\Delta}{\pi} \tag{4.18}$$

with $m = r_{\max}/(\sqrt{3}\Delta)$ for x and setting $\tau_0 = x^2/(2\pi^2) = 7.09 \times 10^{-4}$ for the given choice of Δ and $r_{\max}$.

To calculate F_Z from Eq. (4.16), U_Z is calculated for 30 evenly spaced τ values. These are obtained from Eq. (3.20) where the r-integration is performed numerically from $r = 0$ to $r = r_{\max}$. The remaining term is approximated by the Debye-Hückel potential $\Phi_Z = (Z/r)\exp(-r/\tilde{R}_{\mathrm{D}})$ and the corresponding charge density from the linearized Poisson-Boltzmann equation, $\delta\rho_Z = -Z\exp(-r/\tilde{R}_{\mathrm{D}})/(4\pi\tilde{R}_{\mathrm{D}}^2)$:

$$\frac{1}{2}\int_{r_{\max}}^{\infty} dr r^2 \Phi_Z(r)\delta\rho(r) = -\frac{Z^2}{4\tilde{R}_{\mathrm{d}}} e^{-\frac{2r_{\max}}{\tilde{R}_{\mathrm{D}}}}. \tag{4.19}$$

Potential

Eq. (4.14) is a one-dimensional problem due to the spherical symmetry. As mentioned above, it needs to be solved from $r = 0$ to $r = r_{\max}$. This is done radially by discretizing r, but with finer spacing $\Delta_{\delta\Phi} < \Delta$, which can be chosen since the problem is just one-dimensional. The electron density, calculated only for a few r, is interpolated afterwards using a cubic spline. For the Laplace operator, only the radial part is used:

$$\vec{\nabla}_{\mathrm{r}}^2 = \frac{2}{r}\frac{\partial}{\partial r} + \frac{\partial^2}{\partial r^2}. \tag{4.20}$$

For $r > 0$, the first and second derivatives are calculated using central finite differences with a 4-point stencil and a 5-point stencil, respectively. For the smallest point with $r > 0$, the missing values are "mirrored" at $r = 0$ because of the spherical symmetry. The stencils for the last two r are missing the values for $r > r_{\max}$. These are approximated by using the Debye-Hückel potential, as also performed for the shifted potential when calculating the electron density.

At $r = 0$, L'Hôpital's rule is used:

$$\lim_{r\to 0} \vec{\nabla}_{\mathrm{r}}^2 f(r) = f''(0) + \lim_{r\to 0} \frac{2}{r}\frac{\partial}{\partial r} f(r) = f''(0) + \lim_{r\to 0} \frac{2}{r} f'(r) = 3f''(0) \tag{4.21}$$

For the second derivative, the missing values are again "mirrored".

The total potential Φ_Z is then calculated for all r by adding the factor Z/r. It does not need to be regulated in order to solve the Poisson-Boltzmann equation, because the ions have a positive charge which makes the Boltzmann factor vanish for $r \to 0$, and the electron density is taken from the numerical calculation. In the integral for U_Z, Eq. (3.20), regulation is not needed as well, because the integrand goes to 0 for $r \to 0$. For the calculation of the electron density, the regulation is needed however. This is achieved by replacing $r \to \sqrt{r^2 + \Delta^2/7.7}$ as in Ref. [10].

4.1.3 Example for the potential and density

To see the differences in charge density when comparing the quantum model with the weak screening model, we present here a numerical result for one set of parameters for the helium plasma. The helium density chosen is $n_{\mathrm{He}} = 10^{23}$ cm^{-3} and the temperature $T = 1$keV (i.e. $\beta = 0.027$).

The densities compared are $\delta\rho_{\mathrm{total}} = \rho_{\mathrm{total}} - Z\delta^{(3)}(\vec{r})$, see Eq. (4.13), and the Debye-Hückel density $\rho_{\mathrm{DH}} = \Phi_Z/(4\pi\tilde{R}_{\mathrm{D}}^2)$ obtained from the linearized Poisson-Boltzmann equation Eq. (3.1). The ratio of these densities is plotted against the total potential Φ_Z in Fig. 4.1, as in Ref. [10], Fig. 1. We may interpret the results in the following manner:

- For small r (large Φ_Z), the quantum mechanical nature of the electrons becomes relevant and the electron density approaches a finite value at $r = 0$ instead of diverging.

- For intermediate r (and Φ_Z), the factor $\exp(\beta\Phi_Z)$, to which the electron density is approximately proportional, is larger than its linear approximation, which therefore underestimates the electron density and the absolute value of the charge density.

- For large r and thus small Φ_Z, the linear approximation of the ion contribution is responsible, and overestimates the absolute value of the charge density.

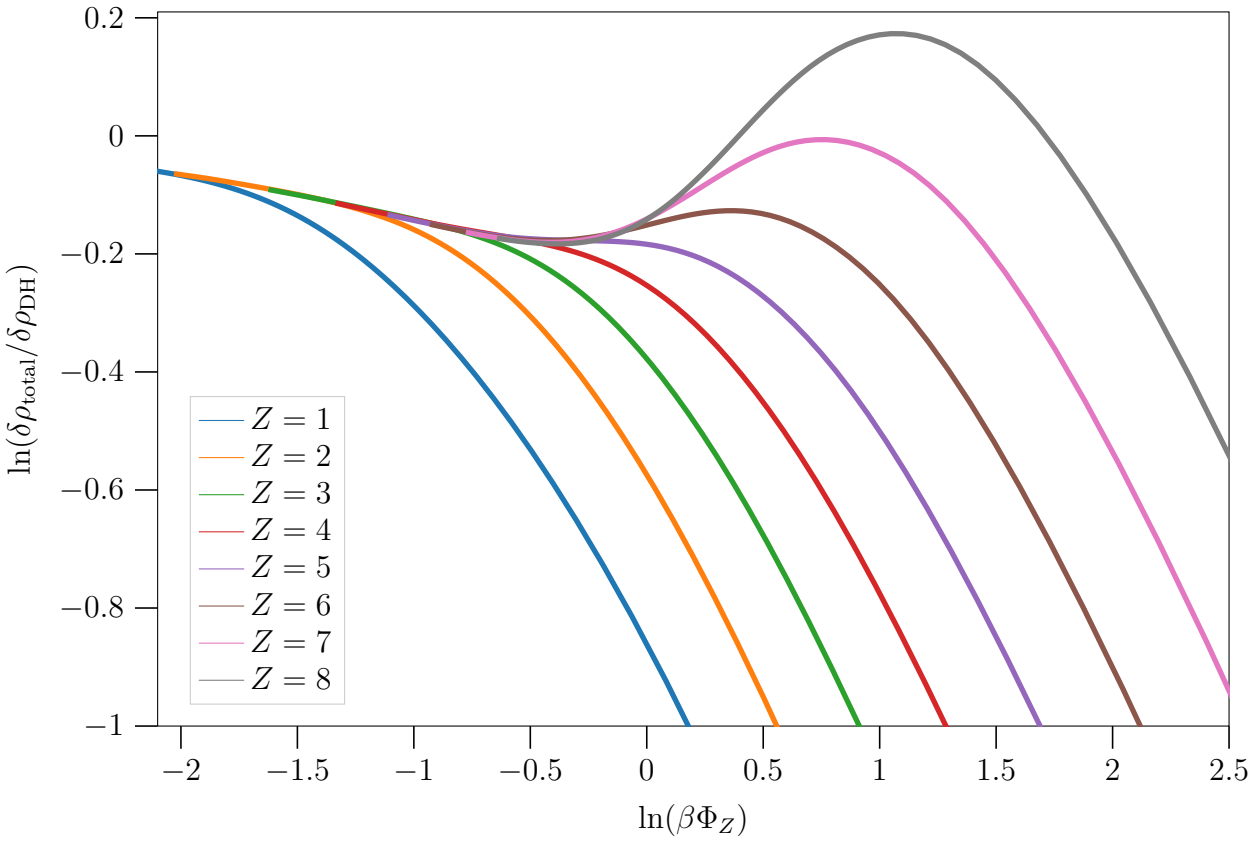

Figure 4.1: Ratio of the quantum mechanical charge density using the full Poisson-Boltzmann equation to the Debye-Hückel density, as a function of the total electrostatic potential Φ_Z, which was used to calculate both densities.

4.2 Kinetic energy shift

Apart from the change in free energy because of the electrostatic energy, the kinetic energy of the electrons also contributes to the change in free energy. This is described in the Appendix of Ref. [10].

4.2.1 Derivation

To calculate the kinetic energy shift from the electron number density $n_e(2\pi\beta)^{3/2}\rho$ (4.12) with the diagonal of the density matrix ρ, the total energy is calculated according to Eq. (4.6) and the sum of $3/2\beta$ and the potential energy V subtracted:

$$\delta K = n_e(2\pi\beta)^{\frac{3}{2}} \int d^3r \left(-\partial_\beta\rho - (\frac{3}{2\beta} + V)\rho\right). \tag{4.22}$$

The partial derivative ∂_β does not include the β-dependence of the potential, because the Hamilton-operator in Eq. (4.6) is regarded as fixed for the calculation of the density matrix. For this part, the Debye-Hückel potential energy $V(r) = -(Z/r)\exp(-r/\tilde{R}_\mathrm{D})$ is used. Thus ∂_β does not act on $\tilde{R}_\mathrm{D}$. To calculate the density matrix analytically, two methods are used: For small r using the eigenstates of a hydrogen-like atom, and for large r using a second order approximation of V. The first method is used below r_0, and the second one above, where $\tilde{R}_\mathrm{D} > r_0 > \sqrt{\beta}$.

Small r

For $Z = 1$, the radial part of the bound states of the hydrogen atom for the non-relativistic Schrödinger equation without spin are given by

$$R_{nl}(r) = \frac{2}{n^{l+2}(2l+1)!}\sqrt{\frac{(n+l)!}{(n-l-1)!}}(2r)^l e^{-\frac{r}{n}} F\left(-n+l+1, 2l+2, \frac{2r}{n}\right) \tag{4.23}$$

with principal quantum number $n \in \mathbb{N}_{>0}$ and orbital angular momentum quantum number $l \in \{\,0, \ldots, n-1\,\}$. The derivation can be found in Ref. [25], §36. F is Kummer's confluent hypergeometric function, defined by

$$F(\alpha, \gamma, z) = \sum_{k=0}^{\infty} \frac{(\alpha)_k}{(\gamma)_k}\frac{z^k}{k!} \tag{4.24}$$

with the rising factorial $(x)_0 \coloneqq 1$ and $(x)_{k+1} \coloneqq (x+k)(x)_k$. If α is a nonpositive integer, as is the case for R_{nl}, the series terminates and becomes a polynomial, here proportional to a Laguerre polynomial. Each (n, l) corresponds to $2l+1$ states with magnetic quantum numbers $m \in \{\,-l, \ldots, l\,\}$. The energy of the states depends only on n and is $E_n = -1/(2n^2)$. The R_{nl} are normalized such that $\int_0^\infty R_{nl}^2(r) r^2\, dr = 1$.

The radial part of the continuum eigenstates of a hydrogen atom is also described in Ref. [25], §36. It can be obtained by substituting $n \to -i/k$. The normalization is chosen such that $\int_0^\infty R_{k'l}(r) R_{kl}(r) r^2\, dr = 2\pi\delta(k'-k)$, which results in

$$R_{kl}(r) = 2k e^{\frac{\pi}{2k}} \frac{|\Gamma(l+1-\frac{i}{k})|}{(2l+1)!}(2kr)^l e^{-ikr} F\left(\frac{i}{k}+l+1, 2l+2, 2ikr\right) \tag{4.25}$$

with the gamma function Γ. The energy is given by $E_n = -1/(2n^2) \to E_k = k^2/2$ and is therefore positive. Each (k, l)-state has a again a degeneracy of $2l+1$.

For $Z > 1$, the probability density can be obtained by replacing $r \to Zr$ and $|R|^2 \to$

$Z^3|R|^2$ for $R \in \{ R_{nl}, R_{kl} \}$. The energies are scaled as $E \to Z^2 E$ for $E \in \{ E_n, E_k \}$.

The unnormalized density matrix can be calculated by expanding the Debye-Hückel potential to the Coulomb potential with a constant correction:

$$V(r) = -\frac{Z}{r} \exp\left(-\frac{r}{\tilde{R}_\mathrm{D}}\right) \approx -\frac{Z}{r} + \frac{Z}{\tilde{R}_\mathrm{D}}. \tag{4.26}$$

According to Eq. (4.8), this implies a constant factor $\exp\left(-\beta Z/\tilde{R}_\mathrm{D}\right)$ in the density matrix. Thus the (unnormalized) spherical symmetrical diagonal of the density matrix is given by

$$\rho(r) = Z^3 e^{-\beta\frac{Z}{\tilde{R}_\mathrm{D}}} \sum_{l=0}^{\infty} \frac{2l+1}{4\pi} \left(\sum_{n=l+1}^{\infty} |R_{nl}(Zr)|^2 e^{\frac{\beta Z^2}{2n^2}} + \frac{1}{2\pi} \int_0^\infty dk |R_{kl}(Zr)|^2 e^{-\beta\frac{Z^2k^2}{2}} \right). \tag{4.27}$$

The factor $1/(4\pi)$ appears because the R_{nl} and R_{kl} are the radial wave functions without the factor 4π in their normalization. Performing a derivative with respect to β yields

$$\begin{aligned} \partial_\beta \rho(r) = &-\frac{Z}{\tilde{R}_\mathrm{D}} \rho(r) + Z^3 e^{-\beta\frac{Z}{\tilde{R}_\mathrm{D}}} \sum_{l=0}^{\infty} \frac{2l+1}{4\pi} \\ &\times \left(\sum_{n=l+1}^{\infty} |R_{nl}(Zr)|^2 \frac{Z^2}{2n^2} e^{\frac{\beta Z^2}{2n^2}} + \frac{1}{2\pi} \int_0^\infty dk |R_{kl}(Zr)|^2 \left(-\frac{Z^2k^2}{2}\right) e^{-\beta\frac{Z^2k^2}{2}} \right), \end{aligned} \tag{4.28}$$

to be used in Eq. (4.22) for the integration from $r = 0$ to $r = r_0$. This then yields the contribution δK_near.

Large r

For large r, V is expanded to second order around a fixed point $\vec{r} = (r, 0, 0)$ with small deviations (x, y, z):

$$V(r + x, y, z) = V(r, 0, 0) + V'x + \frac{1}{2}V''x^2 + \frac{1}{2}\frac{V'}{r}y^2 + \frac{1}{2}\frac{V'}{r}z^2, \tag{4.29}$$

where V' and V'' are the first and second r-derivatives of V, respectively. Thus the differential equation for the density matrix becomes

$$\begin{aligned} &-\partial_\beta \rho((r+x,y,z),(r+x',y',z')) = \\ &-\frac{1}{2}(\partial_x^2+\partial_y^2+\partial_z^2)\rho + (V(r,0,0)+V'x+\frac{1}{2}V''x^2+\frac{1}{2}\frac{V'}{r}y^2+\frac{1}{2}\frac{V'}{r}z^2)\rho. \end{aligned} \tag{4.30}$$

Substituting $x \to x - V'/V''$ yields:

$$\begin{aligned} &-\partial_\beta \rho((r+x-\frac{V'}{V''},y,z),(r+x',y',z')) = \\ &-\frac{1}{2}(\partial_x^2+\partial_y^2+\partial_z^2)\rho + (V(r,0,0)-\frac{V'^2}{2V''}+\frac{1}{2}V''x^2+\frac{1}{2}\frac{V'}{r}y^2+\frac{1}{2}\frac{V'}{r}z^2)\rho. \end{aligned} \tag{4.31}$$

Using the solution for the one-dimensional linear harmonic oscillator with the Hamilton operator

$$\hat{H} = -\frac{1}{2}\partial_x^2 + \frac{\omega^2}{2}x^2, \tag{4.32}$$

for which the diagonal of the density matrix is

$$\rho(x,x) = \sqrt{\frac{\omega}{2\pi\sinh(\omega\beta)}}\exp\left(-\omega x^2\tanh(\frac{1}{2}\omega\beta)\right), \tag{4.33}$$

as shown in Ref. [23], Sec. 2.5, the density matrix can be calculated. The values for ω for the different dimensions are:

- $\omega = i\sqrt{-V''}$ for x,
- $\omega = \sqrt{\frac{V'}{r}}$ for y and z.

For the first case, $\sinh(ix) = i\sin(x)$ and $\tanh(ix) = i\tan(x)$.

The constants in the differential equation simply yield an exponential factor, and thus

the diagonal becomes:

$$\begin{aligned}\rho(r+x-\frac{V'}{V''},y,z) = \\ e^{-\beta V(r,0,0)}e^{\beta\frac{V'^2}{2V''}}\sqrt{\frac{\sqrt{-V''}V'}{r(2\pi)^3\sin\left(\sqrt{-V''}\beta\right)\left(\sinh\left(\sqrt{\frac{V'}{r}}\beta\right)\right)^2}} \\ \times\exp\left(\sqrt{-V''}x^2\tan\left(\frac{1}{2}\sqrt{-V''}\beta\right)\right) \\ \times\exp\left(-\sqrt{\frac{V'}{r}}y^2\tanh\left(\frac{1}{2}\sqrt{\frac{V'}{r}}\beta\right)\right) \\ \times\exp\left(-\sqrt{\frac{V'}{r}}z^2\tanh\left(\frac{1}{2}\sqrt{\frac{V'}{r}}\beta\right)\right).\end{aligned} \tag{4.34}$$

Setting $y = z = 0$ and $x = V'/V''$, the spherical symmetric density matrix becomes

$$\begin{aligned}\rho(r) = e^{-\beta V(r)}e^{\beta\frac{V'^2}{2V''}}\sqrt{\frac{\sqrt{-V''}V'}{r(2\pi)^3\sin\left(\sqrt{-V''}\beta\right)\left(\sinh\left(\sqrt{\frac{V'}{r}}\beta\right)\right)^2}} \\ \times\exp\left(\sqrt{-V''}\frac{V'^2}{V''^2}\tan\left(\frac{1}{2}\sqrt{-V''}\beta\right)\right).\end{aligned} \tag{4.35}$$

Expanding the expression

$$\begin{aligned}\frac{\sqrt{\frac{\sqrt{-V''}V'}{r(2\pi)^3\sin\left(\sqrt{-V''}\beta\right)\left(\sinh\left(\sqrt{\frac{V'}{r}}\beta\right)\right)^2}}}{(2\pi\beta)^{-3/2}} \\ \times e^{\beta\frac{V'^2}{2V''}}\exp\left(\sqrt{-V''}\frac{V'^2}{V''^2}\tan\left(\frac{1}{2}\sqrt{-V''}\beta\right)\right)\end{aligned} \tag{4.36}$$

in β around $\beta = 0$ to order β^3 yields the approximation

$$\rho(r) = (2\pi\beta)^{-\frac{3}{2}}e^{-\beta V}\left(1+\frac{1}{24}\beta^3V'^2-\frac{1}{12}\beta^2(V''+\frac{2}{r}V')\right). \tag{4.37}$$

Using this expression in Eq. (4.22), the contribution to the kinetic energy shift is

$$\delta K_{\text{far}} = n_{\text{e}} 4\pi \int_{r_0}^{\infty} dr r^2 e^{-\beta V} \left(-\frac{1}{8}\beta^2 V'^2 + \frac{1}{6}\beta \left(V'' + \frac{2}{r} V' \right) \right), \tag{4.38}$$

as noted in Ref. [10]. This contribution is negative, but the total kinetic energy shift $\delta K = \delta K_{\text{near}} + \delta K_{\text{far}}$ is positive.

4.2.2 Numerical calculation

For small enough β values, the only numerical difficulties are the infinite series, the R_{kl}-integral and the confluent hypergeometric function F for complex arguments and large z. We can choose a large $n_{\max}$, the n where the series is truncated, without problems, e.g. $n_{\max} = 50 + l$. $l_{\max}$ however needs to be chosen more carefully for smaller Z. For $l < 10$, F can still be evaluated precise enough with a double precision floating point representation with an asymptotic expansion for large z, while for larger l and large k, the precision of the floating point representation needs to be increased. For too large l and small β and Z, the k-integral in Eq. (4.27) and Eq. (4.28) is very oscillatory, thus $l_{\max} = 9$ is used, which gives very similar values even compared to $l_{\max} = 19$, if r_0 is not much larger than $\sqrt{\beta}$.

5 Numerical results

The four methods detailed in the preceding chapters are applied to two reactions: $^{13}\mathrm{C}(\alpha,\mathrm{n})\,^{16}\mathrm{O}$ and $^{7}\mathrm{Li}(\mathrm{d},\alpha)\alpha$. The first reaction takes place in a (almost) pure helium plasma; the second in a deuterium plasma.

Accordingly, the free energies in Ch. 4 need to be calculated for $Z = 1, 2, 3, 4, 6, 8$. The screening factor is calculated for the number densities 10^{18} cm^{-3}, 10^{19} cm^{-3}, 10^{20} cm^{-3}, 10^{21} cm^{-3}, 10^{22} cm^{-3}, 10^{23} cm^{-3} and 10^{24} cm^{-3} of helium and deuterium, respectively. The temperatures are chosen between 50 eV and 1.1 keV.

The results are shown in Fig. 5.1, Fig. 5.2, Fig. 5.3, Fig. 5.4, Fig. 5.5, Fig. 5.6 and Fig. 5.7 for each of the mentioned number densities, respectively. For small temperatures < 100 eV, some very large values were omitted for which the respective model is clearly no longer applicable.

For small densities or large temperatures, all models agree very well. At larger densities and smaller temperatures however, they can differ drastically. This is especially notable for the weak screening model (M1), whose screening factor becomes very large, because the Debye-Hückel radius R_D is very small. Here, the "interaction energy" needs to contain the change in free energy from deforming the "polarization clouds", which is done in the model by Mitler.

The WKB method (M3), which calculates two values proportional to the screened and unscreened reaction rates, also uses the same potential as the Mitler model (M2). The approximation to calculate the change in free energy is dropped however. As can be seen very clearly, this approximation is valid for all considered temperatures and densities for both reactions, where the difference to M3 is insignificant. Thus the latter can be preferred, because it is much easier to use and does not suffer from floating point overflows at small temperatures (where the values in the plots are missing). The method of calculating the screening factor from the change in free energy, which was introduced in M2 and is therefore confirmed in its validity, is also used in M4.

The values for the screening factor f for the same reactions and densities as in the plots are shown in Tab. 5.1, Tab. 5.2, Tab. 5.3, Tab. 5.4, Tab. 5.5 and Tab. 5.6, respectively.

For large densities and small temperatures (small R_D), the density matrix formalism method (M4) is not applicable anymore and encounters numerical difficulties. On the one hand, the assumption that $\beta \ll \tilde{R}_\mathrm{D}$ needed for both parts of M4 no longer holds. On the other hand, the numerical calculation of the density matrix becomes problematic for large β, because the inaccuracies due to the limited grid size, finite spacing and regulation of the Coulomb potential increase for larger β. Also, the Debye-Hückel potential, which is used as initial condition, is not valid anymore under these circumstances. This leads to a calculated electrostatic energy which is much too large. For conditions near those extreme parameters, numerical issues begin to appear and the results could be made more accurate by adjusting the numerical methods in M4 carefully. At intermediate temperatures and densities however, a comparison with experimental results can be expected to provide correct information about the validity of the model. These problems do not appear for plasma screening in stars, because although the densities are indeed large, the temperatures are very high as well [10], which therefore poses no difficulties. Fixing some of these problems may be the subject of future work, as noted in the Outlook.

$n[\mathrm{cm}^{-3}]$	10^{18}	10^{19}	10^{20}	10^{21}	10^{22}	10^{23}	10^{24}
f_M1	1.0020	1.0064	1.0203	1.0657	1.2230	1.8892	7.3865
f_M2	1.0020	1.0063	1.0199	1.0620	1.1890	1.5777	2.9913
f_M3	1.0020	1.0063	1.0199	1.0620	1.1890	1.5777	2.9912
f_M4	1.0020	1.0064	1.0205	1.0680	1.2486	2.0851	6.6391

Table 5.1: Calculated screening factors for different electron densities n considering the reaction $^{13}\mathrm{C}(\alpha,\mathrm{n})\,^{16}\mathrm{O}$ in a helium plasma at $T = 200$ eV.

$n[\mathrm{cm}^{-3}]$	10^{18}	10^{19}	10^{20}	10^{21}	10^{22}	10^{23}	10^{24}
f_M1	1.0003	1.0009	1.0029	1.0092	1.0295	1.0962	1.3352
f_M2	1.0003	1.0009	1.0029	1.0091	1.0284	1.0866	1.2553
f_M3	1.0003	1.0009	1.0029	1.0091	1.0284	1.0866	1.2553
f_M4	1.0003	1.0009	1.0029	1.0092	1.0291	1.0932	1.3033

Table 5.2: Calculated screening factors for different electron densities n considering the reaction $^{7}\mathrm{Li}(\mathrm{d},\alpha)\alpha$ in a deuterium plasma at $T = 200$ eV.

For a prediction of the observables in a nuclear reaction in plasma experiments as envisaged at ELI, we consider the scenarios discussed in Refs. [3, 26].

For the $^{13}\mathrm{C}(\alpha,\mathrm{n})\,^{16}\mathrm{O}$ reaction, the number of neutron events $\mathbb{N}$ per laser pulse with a carbon target thickness of 5 µm in a helium gas (plasma) with a density of 10^{21} cm^{-3} and

$n[\mathrm{cm}^{-3}]$	10^{18}	10^{19}	10^{20}	10^{21}	10^{22}	10^{23}	10^{24}
f_{M1}	1.0005	1.0016	1.0051	1.0162	1.0522	1.1747	1.6626
f_{M2}	1.0005	1.0016	1.0051	1.0160	1.0498	1.1525	1.4632
f_{M3}	1.0005	1.0016	1.0051	1.0160	1.0498	1.1525	1.4632
f_{M4}	1.0005	1.0016	1.0051	1.0162	1.0523	1.1774	1.6837

Table 5.3: Calculated screening factors for different electron densities n considering the reaction $^{13}\mathrm{C}(\alpha,\mathrm{n})\,^{16}\mathrm{O}$ in a helium plasma at $T = 500$ eV.

$n[\mathrm{cm}^{-3}]$	10^{18}	10^{19}	10^{20}	10^{21}	10^{22}	10^{23}	10^{24}
f_{M1}	1.0001	1.0002	1.0007	1.0023	1.0074	1.0235	1.0762
f_{M2}	1.0001	1.0002	1.0007	1.0023	1.0073	1.0228	1.0699
f_{M3}	1.0001	1.0002	1.0007	1.0023	1.0073	1.0228	1.0699
f_{M4}	1.0001	1.0002	1.0007	1.0023	1.0073	1.0233	1.0748

Table 5.4: Calculated screening factors for different electron densities n considering the reaction $^{7}\mathrm{Li}(\mathrm{d},\alpha)\alpha$ in a deuterium plasma at $T = 500$ eV.

a temperature of 100 eV is shown in Table 3 of Ref. [3], which is pretty much the same as for 200 eV. The plasma value there is obtained from the weak screening formula. For the weak screening M1 and the methods M2, M3 and M4, the values calculated in this work can be seen in Tab. 5.7, at a temperature of 200 eV.

For the $^{7}\mathrm{Li}(\mathrm{d},\alpha)\alpha$ reaction, the number of neutron events per laser pulse for a lithium target and deuterium gas (plasma) with a target thickness of 10 µm and the same plasma density as for Tab. 5.7, but with a temperature of 100 eV, is shown in Table 5.2 of Ref. [26]. The weak screening value is shown as well. The values for the other methods are seen in Tab. 5.8. The predictions of all four models are here very close to each other.

These results show that the $^{7}\mathrm{Li}(\mathrm{d},\alpha)\alpha$ reaction is less sensitive to plasma screening effects than the $^{13}\mathrm{C}(\alpha,\mathrm{n})\,^{16}\mathrm{O}$ reaction.

$n[\mathrm{cm}^{-3}]$	10^{18}	10^{19}	10^{20}	10^{21}	10^{22}	10^{23}	10^{24}
f_{M1}	1.0002	1.0006	1.0018	1.0057	1.0182	1.0586	1.1971
f_{M2}	1.0002	1.0006	1.0018	1.0057	1.0179	1.0556	1.1697
f_{M3}	1.0002	1.0006	1.0018	1.0057	1.0179	1.0556	1.1697
f_{M4}	1.0002	1.0006	1.0018	1.0057	1.0180	1.0576	1.1891

Table 5.5: Calculated screening factors for different electron densities n considering the reaction $^{13}\mathrm{C}(\alpha,\mathrm{n})\,^{16}\mathrm{O}$ in a helium plasma at $T = 1.1$ keV.

$n[\mathrm{cm}^{-3}]$	10^{18}	10^{19}	10^{20}	10^{21}	10^{22}	10^{23}	10^{24}
f_{M1}	1.0000	1.0001	1.0003	1.0008	1.0026	1.0083	1.0263
f_{M2}	1.0000	1.0001	1.0003	1.0008	1.0026	1.0082	1.0255
f_{M3}	1.0000	1.0001	1.0003	1.0008	1.0026	1.0082	1.0255
f_{M4}	1.0000	1.0001	1.0003	1.0008	1.0026	1.0082	1.0259

Table 5.6: Calculated screening factors for different electron densities n considering the reaction $^{7}\mathrm{Li}(\mathrm{d},\alpha)\alpha$ in a deuterium plasma at $T = 1.1$ keV.

$\mathbb{N}_{\mathrm{unscreened}}$ $[10^5]$	$\mathbb{N}_{\mathrm{M1}}$ $[10^5]$	$\mathbb{N}_{\mathrm{M2}}$ $[10^5]$	$\mathbb{N}_{\mathrm{M3}}$ $[10^5]$	$\mathbb{N}_{\mathrm{M4}}$ $[10^5]$
4.31	4.59	4.58	4.58	4.60

Table 5.7: Number of neutron events for a carbon target with a thickness of 5 µm in a helium plasma.

$\mathbb{N}_{\mathrm{unscreened}}$ $[10^5]$	$\mathbb{N}_{\mathrm{M1}}$ $[10^5]$	$\mathbb{N}_{\mathrm{M2}}$ $[10^5]$	$\mathbb{N}_{\mathrm{M3}}$ $[10^5]$	$\mathbb{N}_{\mathrm{M4}}$ $[10^5]$
2.13965	2.19598	2.19416	2.19416	2.19428

Table 5.8: Number of neutron events for a lithium target with a thickness of 10 µm in a deuterium plasma.

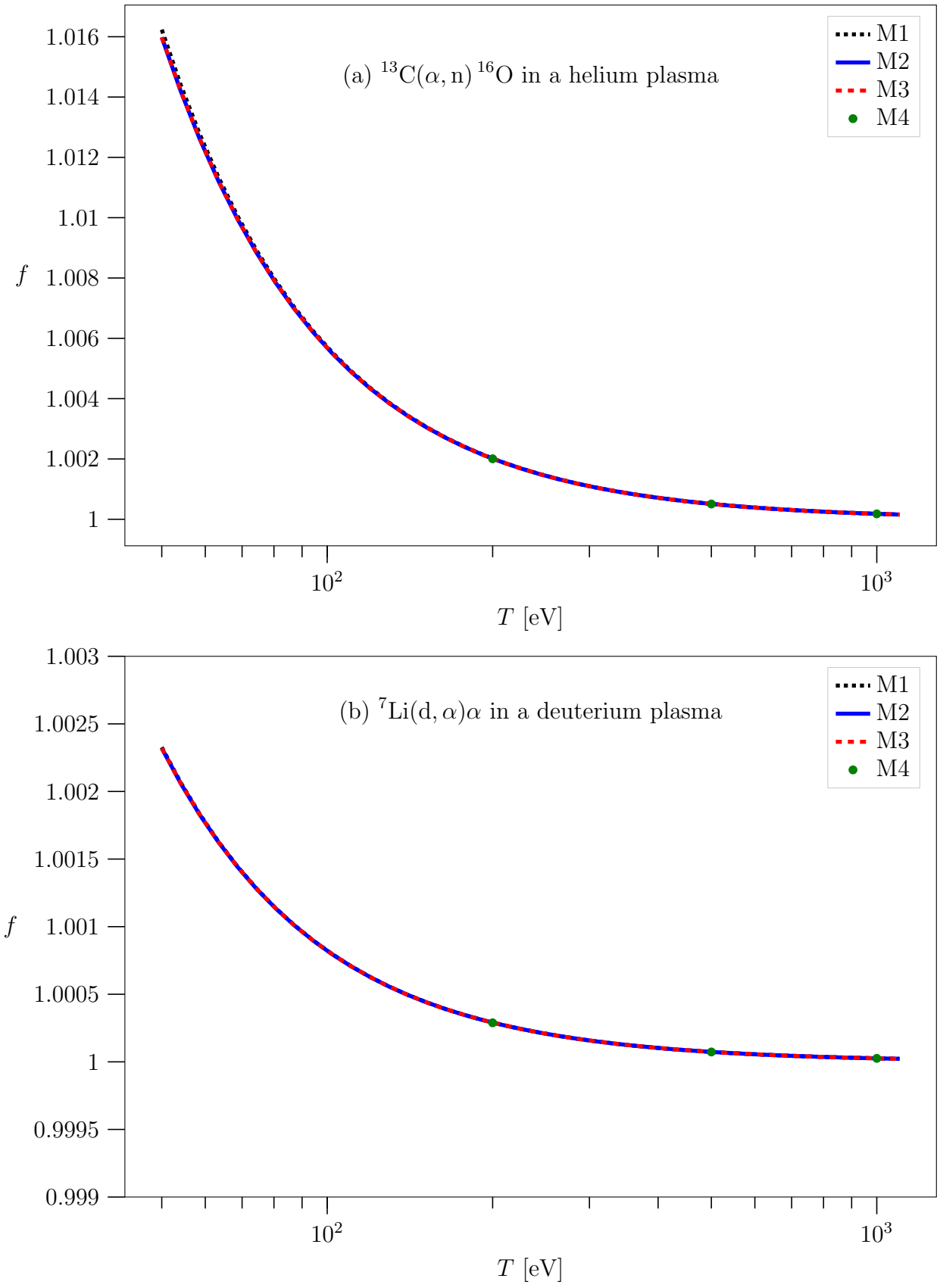

Figure 5.1: Calculated screening factor for a plasma number density of 10^{18} cm^{-3} as a function of plasma temperature T.

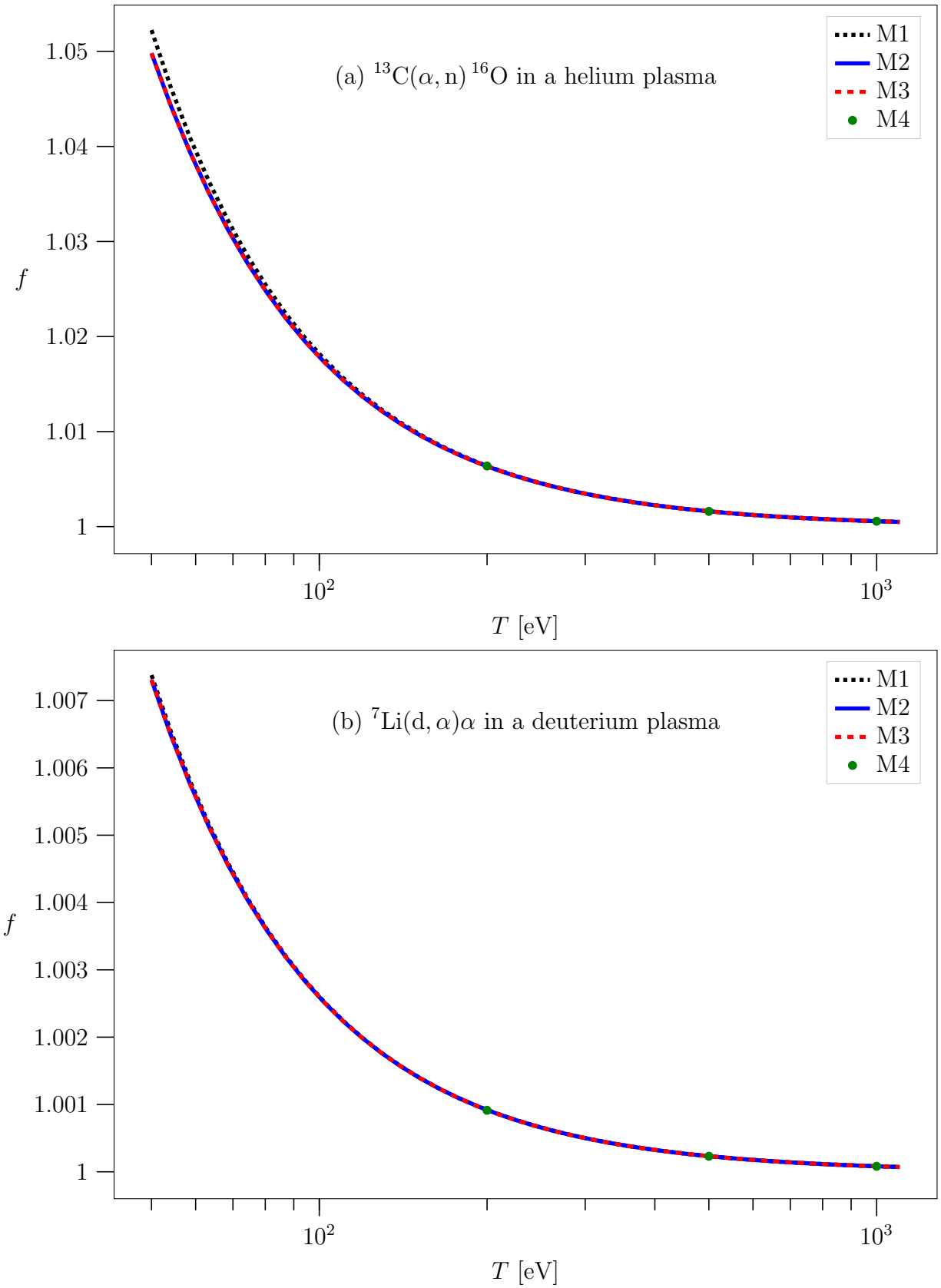

Figure 5.2: Calculated screening factor for a plasma number density of 10^{19} cm^{-3} as a function of plasma temperature T.

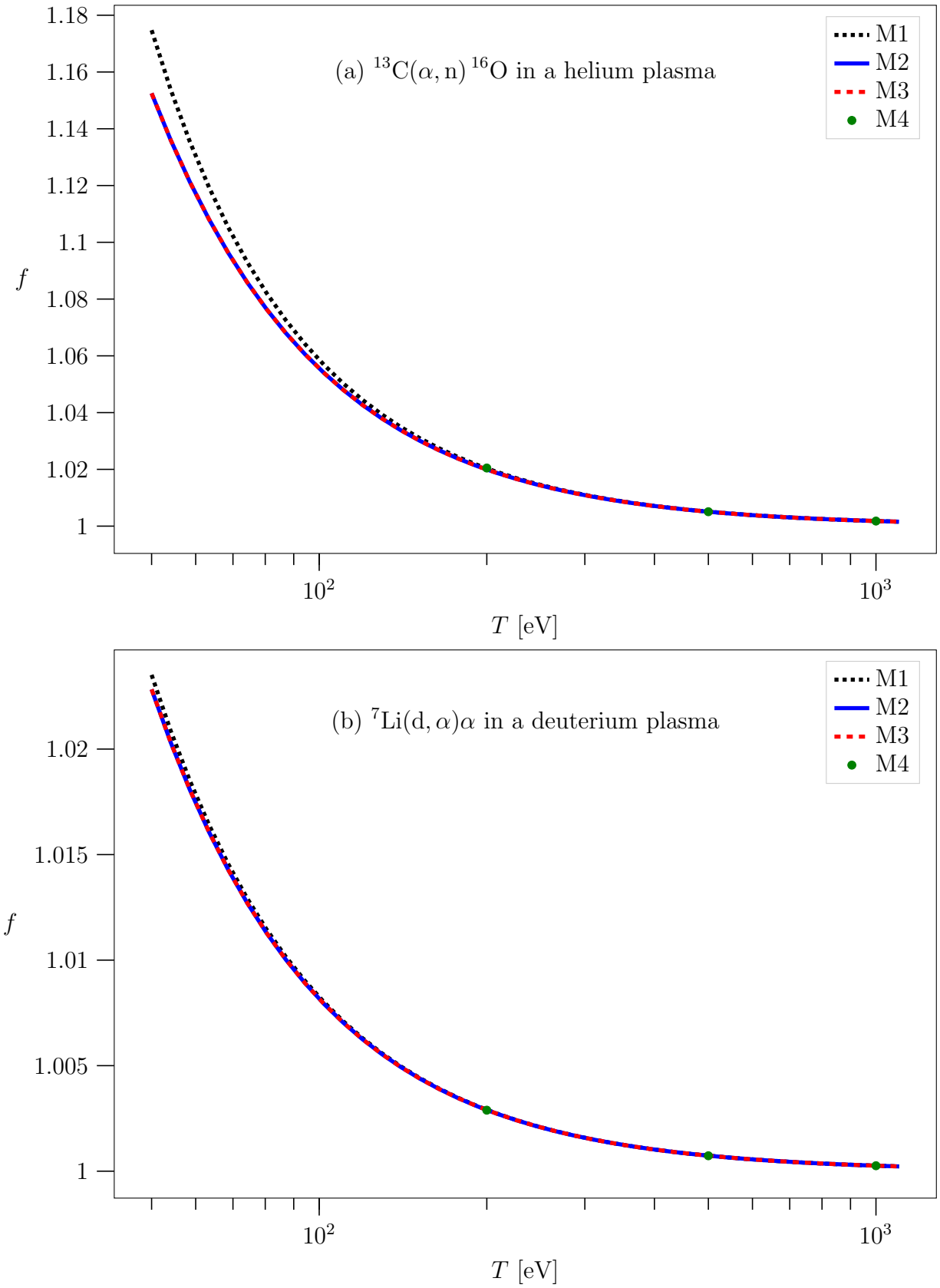

Figure 5.3: Calculated screening factor for a plasma number density of 10^{20} cm^{-3} as a function of plasma temperature T.

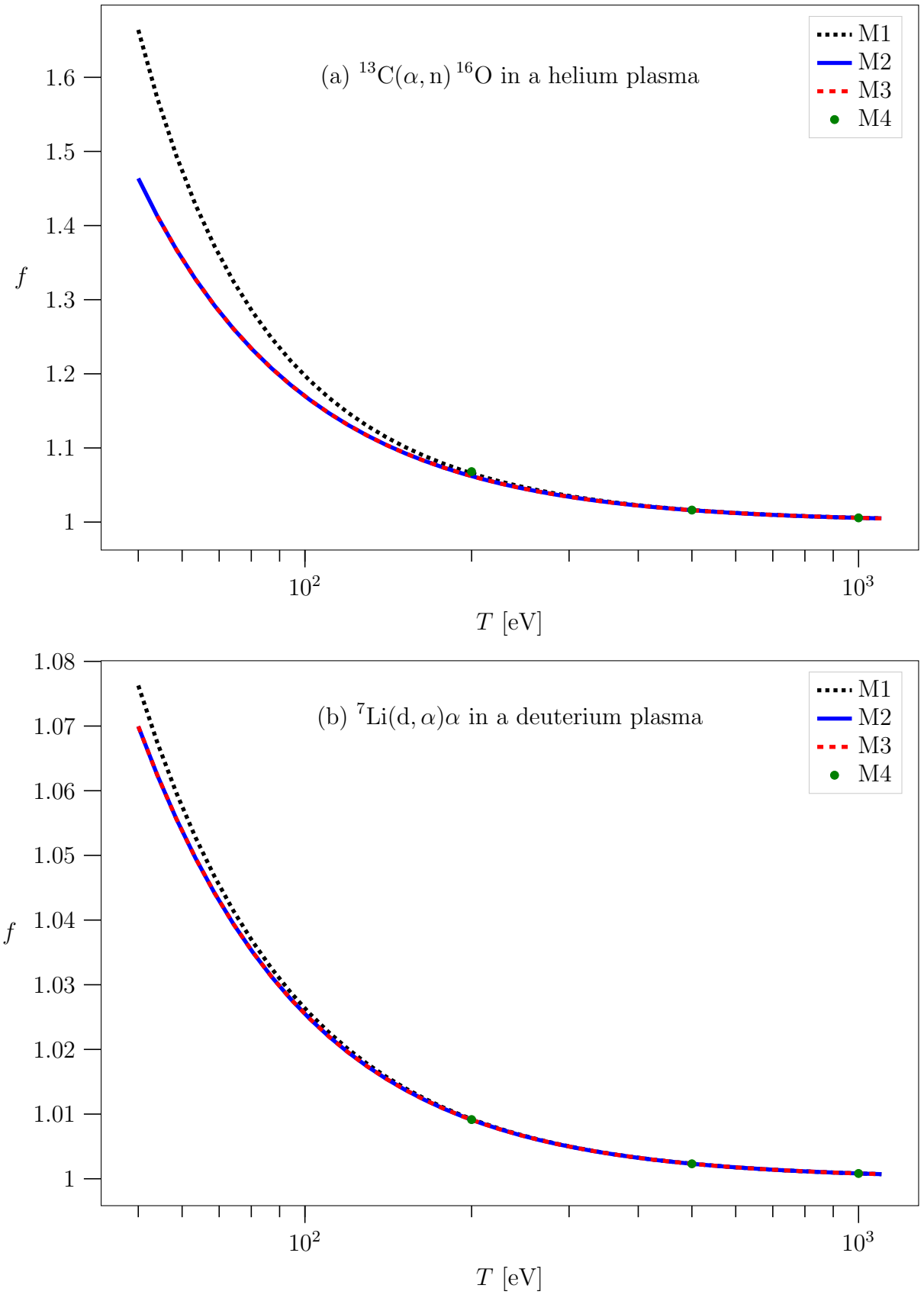

Figure 5.4: Calculated screening factor for a plasma number density of 10^{21} cm^{-3} as a function of plasma temperature T.

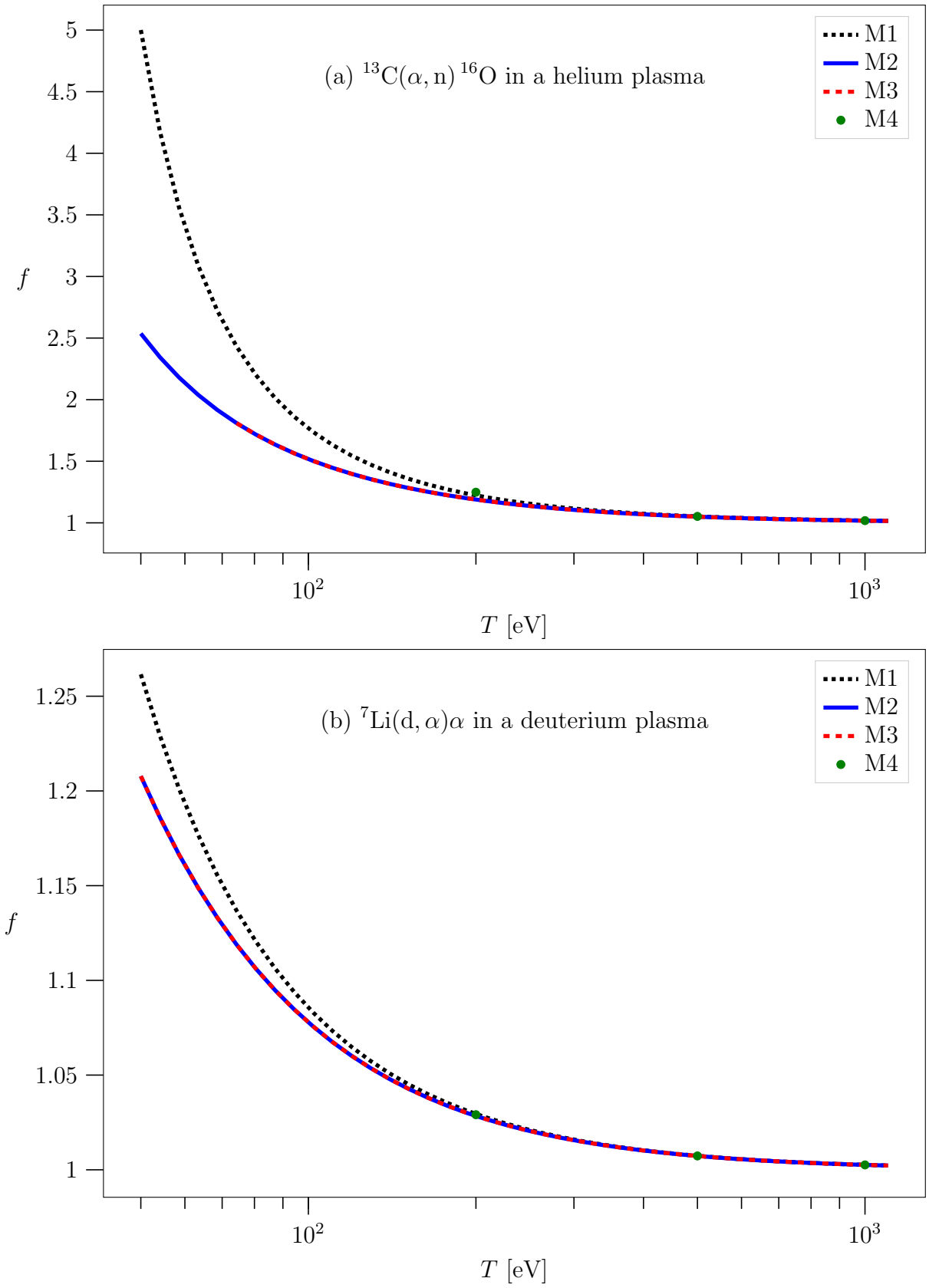

Figure 5.5: Calculated screening factor for a plasma number density of 10^{22} cm^{-3} as a function of plasma temperature T.

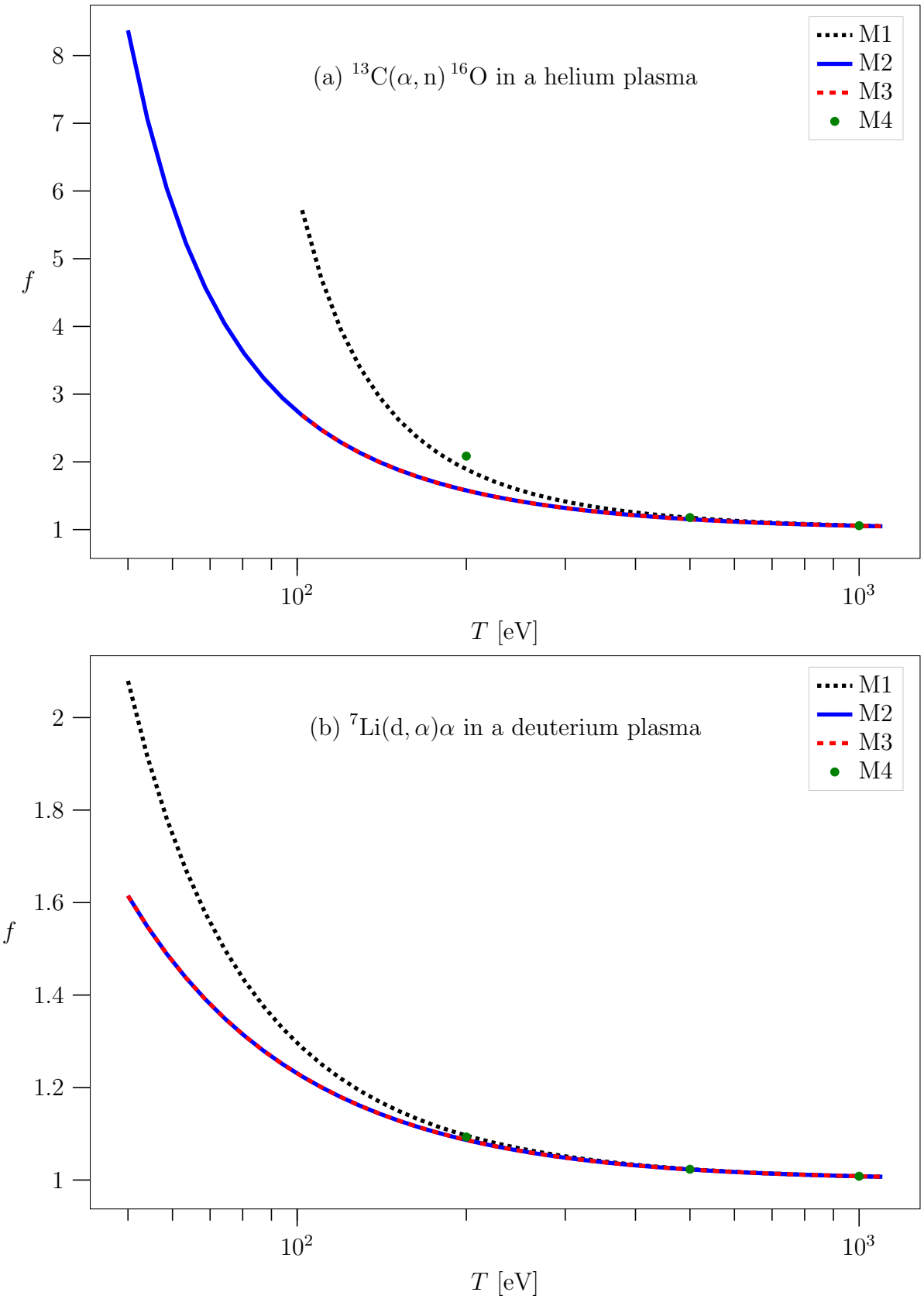

Figure 5.6: Calculated screening factor for a plasma number density of 10^{23} cm^{-3} as a function of plasma temperature T.

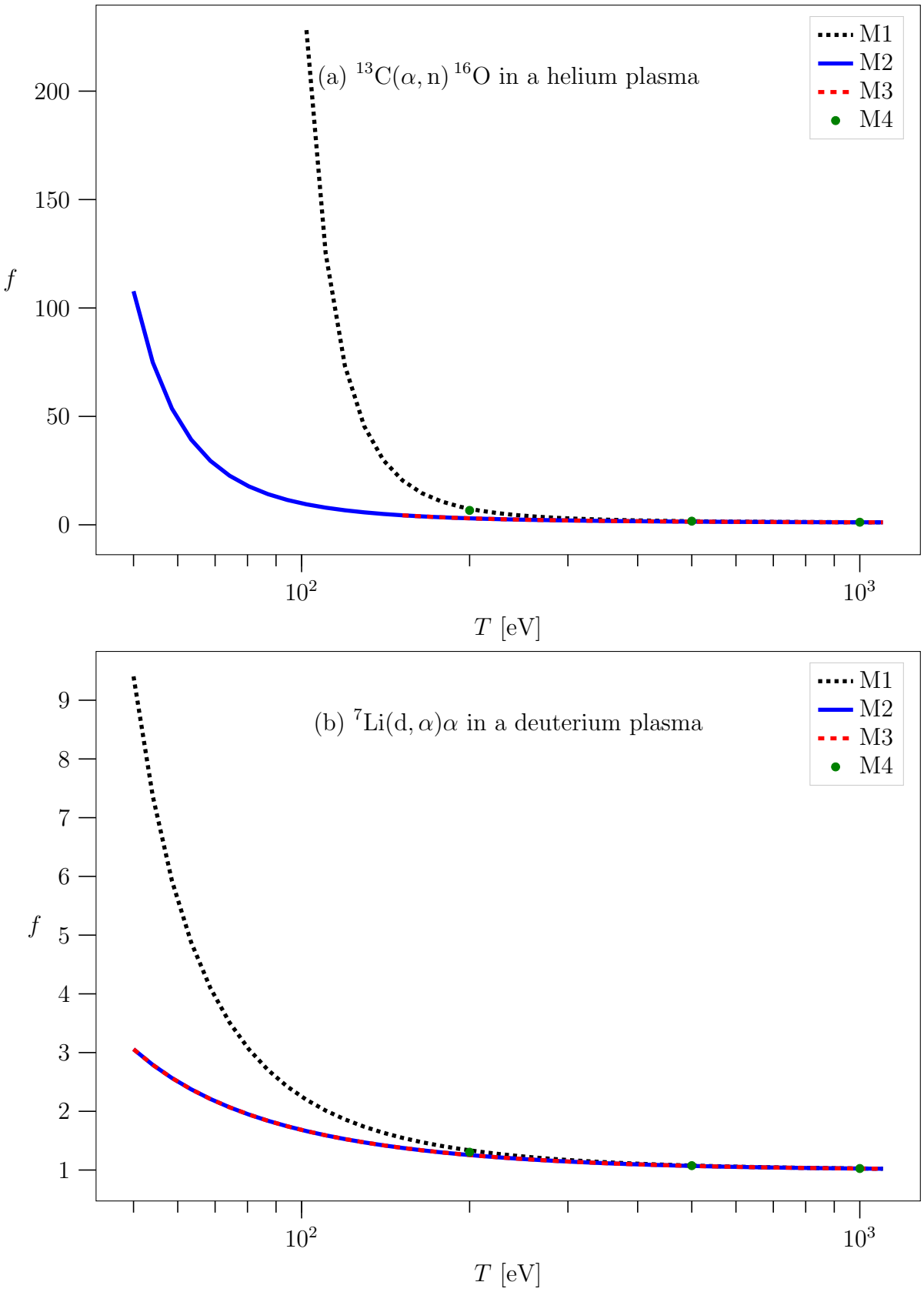

Figure 5.7: Calculated screening factor for a plasma number density of 10^{24} cm^{-3} as a function of plasma temperature T.

6 Summary and Outlook

6.1 Summary

In this work, we have investigated the effects of plasma screening on nuclear reactions. We examined these effects for a PW laser scenario of astrophysical interest, which would enable direct measurements of the same nuclear reaction with and without the plasma environment. Such a future experiment promises to shed light on the validity of different plasma screening models. To this end, four models were considered in detail:

- M1: Salpeter's weak screening model, which is classical except for electron degeneracy,
- M2: Mitler's model, which uses an improved electrostatic potential and calculates the difference in free energy,
- M3: The WKB method, which calculates the penetrability using the WKB approach and integrates the reaction rate explicitly. Its results do not differ significantly from M2 for all cases considered in this work,
- M4: The density matrix formalism method, which calculates the electron density completely quantum mechanically and uses the non-linearized Poisson-Boltzmann equation. It also considers the quantum mechanical kinetic energy shift of the electrons.

These models were employed to calculate the screening enhancement factor for two reactions of astrophysical interest: $^{7}\mathrm{Li}(\mathrm{d},\alpha)\alpha$ in a helium plasma and $^{13}\mathrm{C}(\alpha,\mathrm{n})\,^{16}\mathrm{O}$ in a deuterium plasma for a variety of plasma densities and temperatures. For large temperatures and small densities, all models agree rather well, but for small temperatures and large densities, the prediction of model M1 diverges and model M3 encounters numerical problems due to zero rounding of exponentials. Model M2, which uses the same electrostatic potential as M3, does not encounter such difficulties and does not differ significantly from M3 for all parameters where the latter is applicable. Furthermore, the

approximations made in model M2 to calculate the plasma screening factor from the change in free energy are valid to a high precision, as a comparison with M3 showed. This procedure of using the change in free energy to calculated the screening factor is employed in M4 as well. Notably, the similarity of M2 and M3 shows that the screening factor only depends on the plasma parameters and the electrical charges of the reacting ions, but not significantly on their masses. In its present implementation, M4 encounters numerical instabilities while approaching its validity limit at small temperatures and large densities.

To find out which models and underlying assumptions are correct, a comparison with accurate experimental data is required. Our calculations show that such a comparison should be performed for reactions with high energy in low-temperature plasmas as well as large charge numbers of the reaction ions. Otherwise, the predictions of all four models are very similar making a comparison difficult. Among the two reactions studied in the present work, the differences between the models were larger for the case of the $^{13}\mathrm{C}(\alpha,\mathrm{n})\,^{16}\mathrm{O}$ reaction in a helium plasma than for the $^{7}\mathrm{Li}(\mathrm{d},\alpha)\alpha$ reaction in a deuterium plasma. This is because models M2+M3 and M4 have different approaches for the parameter regime where M1 is no longer applicable, i.e. for large densities, large charge numbers of the reacting ions and small temperatures. Indeed, for the $^{13}\mathrm{C}(\alpha,\mathrm{n})\,^{16}\mathrm{O}$ reaction the considered densities and charge states are larger than for the $^{7}\mathrm{Li}(\mathrm{d},\alpha)\alpha$ reaction and this can be also seen in the larger differences between the screening values calculated with the four models.

6.2 Outlook

Our results in this work can be subject to a number of analytical and numerical improvements, especially concerning M4. The numerical issues of M4 could be improved by refining the first part of the method, e.g. by using the Mitler potential as initial solution, reducing the grid spacing and increasing the number of grid points or regulating the Coulomb potential more carefully. Allegedly, such a procedure would make the time-consuming numerical calculations even more intensive. This would be helpful in extending the possible application of the method to smaller temperatures, larger densities and higher charge numbers of the reacting ions, where the assumptions of M1 are no longer valid, as well as reducing the numerical uncertainty for parameters in the validity range. The kinetic energy shift, which is currently calculated from the Debye-Hückel potential, could also be obtained from the numerical diagonal of the density matrix in

the first part, given a large enough precision.

Considering the comparison with experimental values, the reaction $^{13}\mathrm{C}(\alpha,\mathrm{n})\,^{16}\mathrm{O}$ is more promising than $^{7}\mathrm{Li}(\mathrm{d},\alpha)\alpha$, because the differences between the predictions of the different models are larger, rendering a comparison between them possible. Because the differences between the models depend on the reaction taking place, a different aspect that could involve future work would be finding a better candidate of a sensitive nuclear reaction suitable for a laser-generated plasma experiment, ideally between ions with high charge numbers and in a plasma consisting of heavier ions, as long as the reaction rates are large enough to be measurable.

The present work considers the framework of statistical equilibrium of a plasma, i.e., the two interacting ions should carry with them their full screening cloud during the interaction. However, when looking into the effect of the kinetic energy of the interacting ions on their interaction energy, the issue of *dynamic screening* [27–32] would arise. The basic idea of dynamic screening is that most of the thermal ions in the plasma are much slower than the electrons and the fastest ions. The thermal ions are therefore not able to rearrange themselves as quickly around individual fast ions. Since nuclear reactions require energies much larger than the average thermal energy, the ions involved in nuclear reactions in the plasma are the fast moving ions, which may not be accompanied by their full static screening cloud. It would be interesting to investigate in future works this dynamic screening effect for the experimental detection in laser experiments.

Bibliography

[1] Francis F Chen and Schweickhard E von Goeler. "Introduction to plasma physics and controlled fusion volume 1: Plasma physics". In: *Physics Today* 38 (1985), p. 87.

[2] EE Salpeter. "Electron screening and thermonuclear reactions". In: *Australian Journal of Physics* 7.3 (1954), pp. 373–388.

[3] Yuanbin Wu and Adriana Pálffy. "Determination of plasma screening effects for thermonuclear reactions in laser-generated plasmas". In: *The Astrophysical Journal* 838.1 (2017), p. 55.

[4] Eric G Adelberger et al. "Solar fusion cross sections. II. The p p chain and CNO cycles". In: *Reviews of Modern Physics* 83.1 (2011), p. 195.

[5] P Debye and E Hückel. "De la theorie des electrolytes. I. abaissement du point de congelation et phenomenes associes". In: *Physikalische Zeitschrift* 24.9 (1923), pp. 185–206.

[6] HE Mitler. "Thermonuclear ion-electron screening at all densities. I-Static solution". In: *The Astrophysical Journal* 212 (1977), pp. 513–532.

[7] HE DeWitt, HC Graboske, and MS Cooper. "Screening factors for nuclear reactions. I. General theory". In: *The Astrophysical Journal* 181 (1973), pp. 439–456.

[8] HC Graboske et al. "Screening Factors for Nuclear Reactions. II. Intermediate Screen-Ing and Astrophysical Applications". In: *The Astrophysical Journal* 181 (1973), pp. 457–474.

[9] H Dzitko et al. "The screened nuclear reaction rates and the solar neutrino puzzle". In: *The Astrophysical Journal* 447 (1995), p. 428.

[10] Andrei V Gruzinov and John N Bahcall. "Screening in thermonuclear reaction rates in the sun". In: *The Astrophysical Journal* 504.2 (1998), p. 996.

[11] S Fukuda et al. "Solar B 8 and hep Neutrino Measurements from 1258 Days of Super-Kamiokande Data". In: *Physical Review Letters* 86.25 (2001), p. 5651.

[12] Q Retal Ahmad et al. "Measurement of the Rate of $\nu_e + d \rightarrow p + p + e^-$ Interactions Produced by B 8 Solar Neutrinos at the Sudbury Neutrino Observatory". In: *Physical Review Letters* 87.7 (2001), p. 071301.

[13] D Mascali et al. "Colliding laser-produced plasmas: a new tool for nuclear astrophysics studies". In: *Radiation Effects & Defects in Solids: Incorporating Plasma Science & Plasma Technology* 165.6-10 (2010), pp. 730–736.

[14] *ELI-beamlines L4 beam line webpage*. `https://www.eli-beams.eu/en/facility/lasers/laser-4-10-pw-2-kj/`. 2018.

[15] A Casner et al. "LMJ/PETAL laser facility: Overview and opportunities for laboratory astrophysics". In: *High Energy Density Physics* 17 (2015), pp. 2–11.

[16] *LULI2000 laser system webpage*. `https://portail.polytechnique.edu/luli/en/facilities/luli2000/luli2000-laser-system`. 2018.

[17] *Central Laser Facility Vulcan laser webpage*. `https://www.clf.stfc.ac.uk/Pages/Vulcan-laser.aspx`. 2018.

[18] *Petawatt High-Energy Laser for heavy Ion Experiments—PHELIX webpage*. `https://www.gsi.de/en/work/research/appamml/plasma_physicsphelix/phelix.htm`. 2018.

[19] *National Ignition Facility & Photon Science webpage*. `https://lasers.llnl.gov/`. 2018.

[20] *The Magajoule Laser facility webpage*. `http://www-lmj.cea.fr/index-en.htm`. 2018.

[21] F Negoita et al. "Laser driven nuclear physics at ELI–NP". In: *Romanian Reports in Physics* 68.Supple (2016), S37–S144.

[22] Matthias Bartelmann et al. *Theoretische Physik*. Springer-Verlag, 2014.

[23] RP Feynman. *Statistical Mechanics, A Set of Lectures, California, Institute of Technology*. 1972.

[24] Sara Zahedi and Anna-Karin Tornberg. "Delta function approximations in level set methods by distance function extension". In: *Journal of Computational Physics* 229.6 (2010), pp. 2199–2219.

[25] LD Landau and EM Lifshitz. "Quantum mechanics, vol. 3". In: *Course of theoretical physics* 3 (1977).

[26] Antonia Schneider. *Nucleosynthesis in Astrophysical Plasmas*. Bachelor Thesis, Heidelberg University, 2016.

[27] Nir J Shaviv and Giora Shaviv. "The Electrostatic Screening of Thermonuclear Reactions in Astrophysical Plasmas. I." In: *The Astrophysical Journal* 468 (1996), p. 433.

[28] Giora Shaviv and Nir J Shaviv. "Is there a dynamic effect in the screening of nuclear reactions in stellar plasmas?" In: *The Astrophysical Journal* 529.2 (2000), p. 1054.

[29] Nir J Shaviv and Giora Shaviv. "The electrostatic screening of nuclear reactions in the Sun". In: *The Astrophysical Journal* 558.2 (2001), p. 925.

[30] John N Bahcall et al. "The Salpeter plasma correction for solar fusion reactions". In: *Astronomy & Astrophysics* 383.1 (2002), pp. 291–295.

[31] Dan Mao, Katie Mussack, and Werner Däppen. "Dynamic screening in solar plasma". In: *The Astrophysical Journal* 701.2 (2009), p. 1204.

[32] Katie Mussack and Werner Däppen. "Dynamic screening correction for solar pp reaction rates". In: *The Astrophysical Journal* 729.2 (2011), p. 96.

Acknowledgements

I would like to thank my supervisors PD Dr. Adriana Pálffy-Buß and Dr. Yuanbin Wu for their suggestions and help.

Erklärung

Ich versichere, dass ich diese Arbeit selbstständig verfasst und keine anderen als die angegebenen Quellen und Hilfsmittel benutzt habe.

Heidelberg, den 12.09.2018,